Miniaturization of Interferometric Optical Gyroscopes: A Review

Francesco Dell'Olio, *Senior Member, IEEE*, Teresa Natale, Yen-Chieh Wang, and Yung-Jr Hung, *Member, IEEE*

***Abstract*—Gyroscopes are inertial sensors whose field of application is rapidly expanding. The growing interest in autonomous systems, CubeSats as well as their constellations, and unmanned vehicles is stimulating a strong interest in miniaturized gyroscopes for integration in inertial units with a volume smaller than 100 cm^3. Some of these applications require gyroscopes that are highly immune to disturbances, especially vibrations, mechanical shocks, and radiation. In these application contexts, the use of microelectromechanical gyroscopes is often avoided in favor of sensors without moving parts, such as optical gyroscopes based on the Sagnac effect. The technology of interferometric optical gyroscopes is currently considered to be potentially capable of enabling the development of highly innovative angular velocity sensors, which are simultaneously inertial grade and miniaturized. This article critically examines the scientific and research and development activity aimed at miniaturization of interferometric optical gyroscopes, focusing on recent results, perspectives, and physical limitations. Interferometric optical gyroscopes with dimensions similar to those of microelectromechanical gyroscopes and better performance than the latter in terms of immunity to disturbances have not yet been demonstrated, but this article shows how this goal could be realistically achieved in the medium term through the use of integrated microphotonics. This article compares the technology being analyzed with the competitive technologies, highlighting their strengths and limitations.**

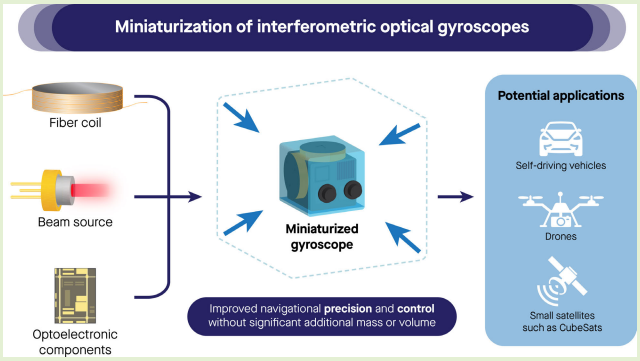

***Index Terms*— Gyroscope, interferometry, miniaturized sensor, optoelectronic sensor.**

I. Introduction

GYROSCOPES are sensors with different levels of accuracy that are capable of measuring the angular velocity of a body around one or more axes with respect to an inertial reference frame [1].

They are now vastly used in numerous application fields, including aerospace, defense, consumer electronics, robotics, healthcare, and the automotive industry. The most traditional application of gyroscopes, especially those with high performance, is within strapdown inertial navigation systems (INSs) [2], where the gyroscopes provide accurate measurements of angular velocity and autonomous navigation capabilities by continuously tracking the orientation and movement of a vehicle or a platform. In INSs, the gyroscopic measurements are integrated over time to estimate the platform orientation and angular displacement. These estimates are then used to calculate the position and velocity of the vehicle through an inertial navigation algorithm, typically employing Kalman filtering techniques.

The main physical effects exploited in the gyroscopes currently on the market are the Coriolis and Sagnac effects. The former causes energy coupling between two mechanical resonant modes only due to an applied external rotation [3]. The latter occurs when two counterpropagating light beams travel along a closed path in a rotating frame, causing a phase shift between the light waves [4]. The Coriolis effect is exploited in Coriolis vibratory gyroscopes, a vast group of sensors, including silicon- and quartz-based microelectromechanical system (MEMS) gyroscopes [5], hemispherical resonant gyroscopes (HRGs) [6], and other gyroscopes based on high-quality metal resonators [7], [8].

MEMS gyroscopes are still not used in navigation applications due to some limitations in their performance that

Manuscript received 2 September 2023; revised 20 October 2023; accepted 20 October 2023. Date of publication 30 October 2023; date of current version 14 December 2023. This work was supported in part by the National Science and Technology Council, Taiwan, under Grant 111-2223-E-110-002-MY4. The associate editor coordinating the review of this article and approving it for publication was Dr. Rui Min. *(Corresponding author: Francesco Dell'Olio.)*

Francesco Dell'Olio and Teresa Natale are with the Micro Nano Sensor Group, Polytechnic University of Bari, 70125 Bari, Italy (e-mail: francesco.dellolio@poliba.it; t.natale@phd.poliba.it).

Yen-Chieh Wang and Yung-Jr Hung are with the Department of Photonics and Miniaturized Photonic Gyroscope Research Center (MPGRC), National Sun Yat-sen University, Kaohsiung 80424, Taiwan (e-mail: wangjay1214@g-mail.nsysu.edu.tw; yungjr@mail.nsysu.edu.tw).

Digital Object Identifier 10.1109/JSEN.2023.3327217

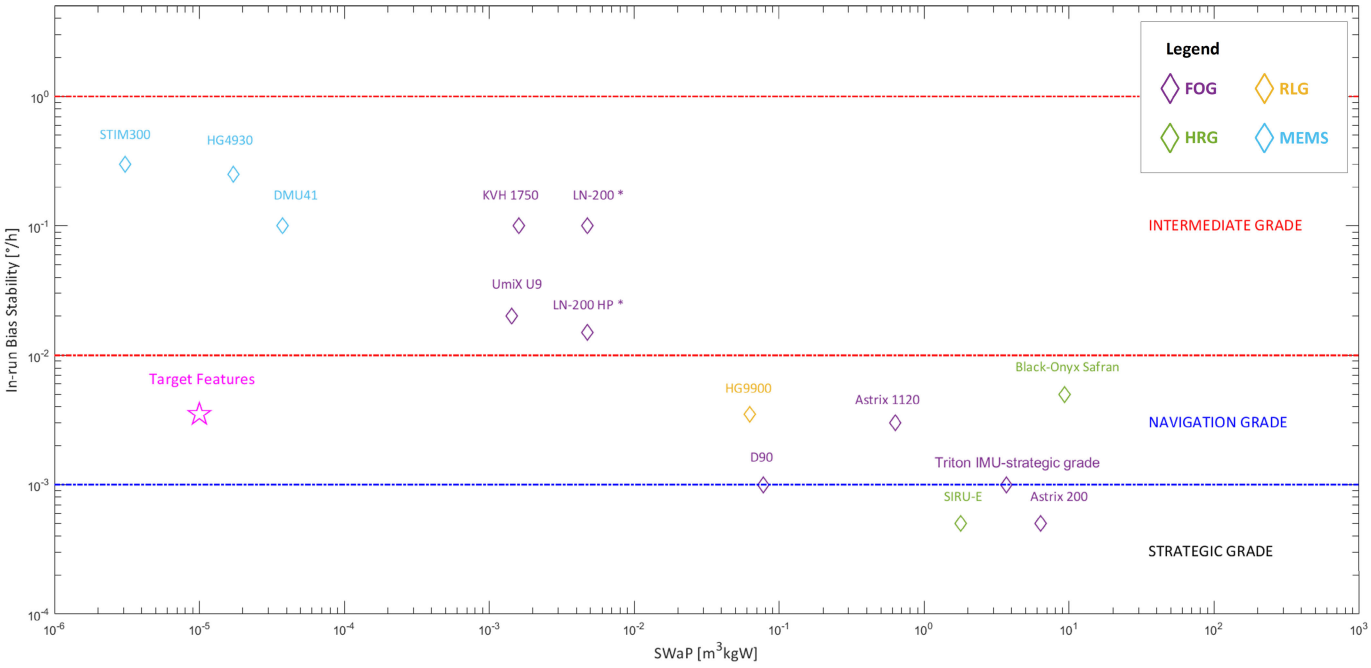

Fig. 1. Estimated BIS and IMU/INS SWaP of some for the gyroscope on the market. The star indicates the target features of an IMU integrating a miniaturized navigation-grade gyroscope. (*) BIS estimated as one order of magnitude less than bias repeatability, i.e., the initial bias error obtained between successive switch OFF–switch ON, at constant temperature.

are very difficult to overcome. HRGs can achieve very high performance but are usually bulky and costly. The gyroscopes based on the Sagnac effect that have reached the market are the fiber optic gyroscope (FOG) [9], interferometric gyroscope based on a long fiber coil in which the counterpropagating beams travel, and ring laser gyroscope (RLG) [10], which is based on a He–Ne ring laser where two resonating modes are excited. Both the FOG and the RLG are bulk sensors with a cost that is usually not compatible with applications outside the inertial navigation domain. The availability on the market of low-cost silicon-based MEMS gyroscopes based on the Coriolis effect has triggered new gyroscope applications in the fields of virtual and augmented reality, robotics, and the Internet of Things, but there still exist potential application domains, e.g., navigation and control systems of autonomous vehicles and attitude and orbit control of CubeSats, that have requirements that are not fully compliant with the gyroscopes on the market. This market need motivates a research effort aimed at filling the gap through several approaches, including scaling of well-established bulk gyroscope technologies, mainly optical gyroscopes and HRGs.

Gyroscopes are usually classified according to their performance, especially in terms of the in-run bias stability or bias instability (BIS): consumer rate grade (BIS $>$ 100 °/h), industrial rate grade (BIS = 10–100 °/h), tactical grade (BIS = 1–10 °/h), intermediate grade (BIS = 0.01–1°/h), navigation grade (BIS $<$ 0.01°/h), and strategic grade (BIS $<$ 0.001°/h). There are numerous other parameters quantifying the gyroscope performance, including the angle random walk (ARW), a measure of the sensor wideband noise, and the scale factor stability. Navigation grade requires ARW $<$0.005 °/$\sqrt{\text{h}}$ and scale factor stability on the order of 10 ppm, while strategic grade demands ARW $<$0.0003 °/$\sqrt{\text{h}}$ and scale factor stability of a few ppm.

Rate-grade gyroscopes are very inexpensive and extremely miniaturized, with a volume of less than 1 cm^3, while strategic-grade gyroscopes are very bulky, and their volume is commonly larger than several thousand cm^3. Navigation-grade gyroscopes are also typically bulky and expensive, which prevents their application in contexts that would benefit from their performance but have stringent requirements on cost and size. Referring to some examples of inertial measurement units (IMUs) or INSs on the market that have at least intermediate-grade performance, Fig. 1 shows an estimation of both the gyroscope BIS and the size, weight, and power (SWaP) budget of the whole unit [11], [12], [13], [14], [15], [16], [17], [18], [19], [20], [21], [22], [23]. As the main performance parameter, we consider the BIS, i.e., the measure of how the bias will drift during operation over time at a constant temperature. The plot clearly highlights that miniaturized IMUs with volume $<$100 cm^3 and SWaP $<10^{-4}$ m^3·kg·W are all based on MEMS gyroscopes with BIS $>$0.1°/h. Better performance inevitably requires larger volumes. IMUs/INSs integrating optical or hemispherical gyroscopes have a volume that ranges from some hundreds of cm^3 to a few tens of thousands of cm^3 and SWaP budgets in the range of 0.001–10 m^3·kg·W. Navigation-grade IMUs/INSs have a minimum volume of a few thousands of cm^3 and a minimum SWaP budget on the order of 0.1 m^3·kg·W.

One of the major technological advances in the last 70 years has been miniaturization, which allows many devices and components performing operations with different complexity levels to be packed into a very small area at a cost an order of magnitude lower than that of macroscopic equipment

performing the same functions. Miniaturization is the key driver in the exponential development of microelectronics and nanoelectronics described by Moore's law [24] but also plays a crucial role in sensing technology. Sensor miniaturization enables cost reduction and new applications and is unanimously considered a crucial research and development objective. In addition, in the field of gyroscopes, one of the main research challenges is miniaturization. In particular, recent research has focused on reducing the SWaP budget, which also influences the cost of navigation-grade sensors. Navigation-grade gyroscopes that can be integrated in IMUs with a volume of approximately 100 cm^3 and an SWaP budget on the order of 10^{-5} $m^3 \cdot kg \cdot W$ would enable new compact navigation systems or improve the performance of existing systems with a vast spectrum of application domains. The most explored way to achieve this goal is through performance enhancement of MEMS gyroscopes, which are intrinsically miniaturized. Considering the prototypes at the medium/low technology readiness level (TRL), the BIS of the state-of-the-art is on the order of 0.01°/h (typically at constant room temperature) [25], [26], at the border between intermediate and navigation grades. Although the research and development effort aimed at demonstrating and transferring to market MEMS navigation-grade gyroscopes has been impressive, to our knowledge, the application of such gyroscopes in real-world INSs intended for aerospace and defense is limited to only a few examples, especially in the field of autonomous vehicles [27], [28].

Alternative approaches that have been explored to demonstrate small navigation-grade gyroscopes are based on the miniaturization of optical sensors, exploiting the Sagnac effect. Miniaturization of navigation-grade resonant gyroscopes based on active or passive resonators has been demonstrated to be extremely challenging due to a wide range of physical effects, including lock-in and mode competition in solid-state ring lasers and backscattering and Kerr nonlinearity in high-quality-factor passive ring resonators. Miniaturization of interferometric optical gyroscopes, which is the topic of this review article, is one of the most promising ways to achieve the above scientific and technological goal. The key advantages of interferometric optical gyroscopes are their all-solid-state design, high immunity to external disturbances, wide dynamic range, and flexible design. All these features make such gyroscopes very interesting for all applications demanding both miniaturization and high performance.

This article critically analyzes the various options available to miniaturize interferometric optical gyroscopes currently on the market and compares the approaches currently under study with other competitive approaches based on optical, electromechanical, and quantum technologies. The rest of this article is organized as follows. The principle of interferometric gyroscopes is introduced in Section II. The strategies for miniaturizing such sensors are presented in Section III, and the comparison to competing technologies is discussed in Section IV. Section V is focused on the conclusion and discussion.

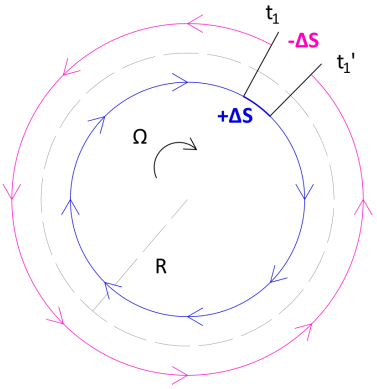

Fig. 2. Optical path changes due to rotation. The blue co-rotating path is increased (+ΔS), and the magenta counter-rotating path is decreased (−ΔS).

II. Interferometric Gyros

Interferometric gyroscopes are the main topic of this article. This section provides an overview of their operating principle and a block diagram, highlighting the noise sources and the countermeasures to mitigate them [29].

A. Sagnac Effect

All optical gyroscopes are based on the Sagnac effect, in which a phase difference arises between two light beams that originate from a single light beam and propagate in opposite directions along a rotating closed loop [30], [31]. The effect is observed in both ring interferometers and ring cavities. The Sagnac effect is a relativistic effect based on the Fresnel–Fizeau drag effect, defined in (1), that explains the light velocity in a medium

$$v = \frac{c}{n} + \left(1 - \frac{1}{n^2}\right) v_{\text{medium}}. \tag{1}$$

where c is the speed of light in vacuum, n is the medium refractive index, and v_{medium} is the velocity in the medium.

A ring interferometer, which is exploited in interferometric gyroscopes, is a type of interferometer that uses a closed loop as the optical path. The input light beam, collimated inside the system, is split into two different beams that propagate in opposite directions along the closed circular path. If the system is at rest, then the two beams follow the same optical path at the same time. When the system is rotating, the two beams travel different optical distances and arrive at the detector out of phase due to the delay accumulated along the geometrical paths, as shown in Fig. 2.

The rotation induced phase shift $\Delta\phi_R$ is given by

$$\Delta\phi_R = \frac{4\omega}{c^2} \mathbf{A} \cdot \mathbf{\Omega}. \tag{2}$$

where $\mathbf{\Omega}$ refers to the rotation rate vector and $\mathbf{A}$ is the effective area vector of the enclosed path

$$\mathbf{A} = \frac{1}{2} \oint \mathbf{r} \times \mathbf{dr}. \tag{3}$$

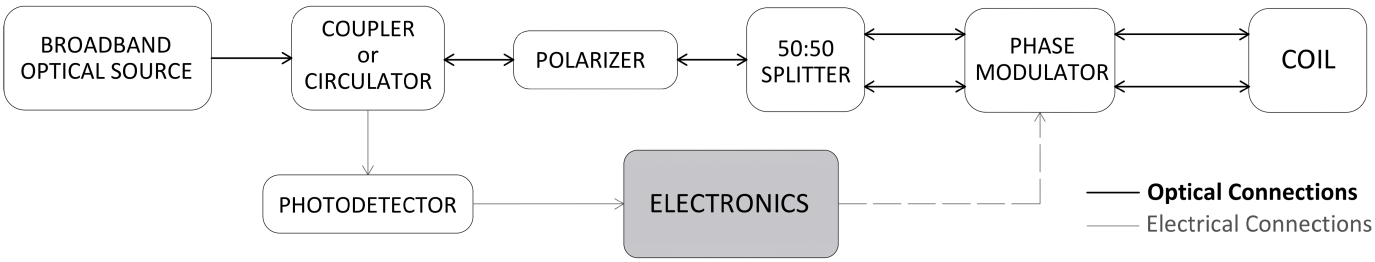

Fig. 3. Interferometric optical gyroscope: block diagram.

where **A** is defined as a line integral, where **r** is the radial coordinate vector. The Sagnac effect can be enhanced with a multiturn path because, as shown in (2), it is proportional to the flux of the rotation rate vector **Ω**. In FOGs, a closed-loop optical path is used as a sensitive element. In the case of an interferometric gyroscope, based on a fiber or waveguide coil with length L and diameter D, $\Delta\phi_R$ can be written as

$$\Delta\phi_R = \frac{2\pi L D}{\lambda_C}\Omega. \tag{4}$$

Equations (2) and (4) are valid if light propagates in vacuum or in a medium, as in the case of the FOG.

The ring optical cavities where light recirculates many times around the resonant path can be either active or passive, depending on whether they include an optical gain medium. The Sagnac effect is observed in these resonators as a small frequency difference between two counterpropagating resonant modes supported by the cavity. The difference, which is independent of the refractive index of the medium filling the cavity, is

$$\Delta f_R = \frac{4A}{\lambda P}\Omega. \tag{5}$$

where A is the area enclosed by the ring cavity, P is the cavity perimeter, and λ is the resonance wavelength of the modes at rest. In an active ring laser cavity, such as that used in He–Ne RLG, Δf_R can be measured by making the two laser-generated counterpropagating beams interfere, while in a passive cavity such as that implemented by a fiber ring resonator, Δf_R can be measured by either phase modulation or frequency modulation spectroscopy [32].

B. Block Diagram

Fig. 3 shows the basic block diagram of an interferometric optical gyroscope. All the blocks represent the gyroscope components.

The light source is a broadband optical source that is useful for attenuating some noise effects by reducing the coherence of the emitted light. The emitted light is coupled by an optical coupler, or a circulator, to achieve a complete reciprocal configuration. The implementation of a reciprocal configuration in interferometric optical gyroscopes avoids the parasitic phase difference between the two optical waves. A polarizer is used at the common reciprocal port to equalize the phase of the two counterpropagating waves at rest. Without the polarizer, in a ring interferometer, the two waves that propagate in opposite directions may have different states of polarization. Because of birefringence, they should not see the same refractive index, which yields a spurious difference in phase. After passing through the polarization filter, the beam is ideally divided into two equal beams by a 50:50 splitter. A phase modulation is applied to the two waves to realize higher sensor sensitivity. The sensitive element is represented by the coil.

The optical signal is converted at the photodetector into an electrical signal that is processed by the electronics to obtain the angular velocity measurement. In open-loop sensors, the angular velocity is readout by processing the photodiode-generated signal, while in closed-loop gyroscopes, the electronics generate a feedback signal compensating for the rotation effect, and the angular velocity is estimated based on the magnitude of the feedback signal. The dotted line in Fig. 3 refers to the closed-loop configuration.

The most typical implementation of the block diagram in Fig. 3 is the FOG, where the coil is a fiber coil made of a polarization-maintaining (PM) single-mode low-loss fiber and the polarizer, splitter, and phase modulator are all integrated on a lithium niobate ($LiNbO_3$) chip, which is also referred to as a multifunctional integrated optical chip (MIOC).

To ensure the correct operation of the angular velocity sensor, the sources of noise that cause an incorrect reading of the phase variation between the two beams counterpropagating in the fiber optic coil due to the Sagnac effect must be attenuated. The shot noise effect at the photodiode is related to the randomly distributed photons at the detector, which yield fluctuations in the output current. Shot noise is one of the main limitations of FOGs, and this type of noise is not negligible and must be properly managed.

The polarization coupling noise, Rayleigh backscattering, Shupe effect, Kerr effect, Faraday effect in the fiber coil, and center wavelength drift at the broadband optical source are the primary sources of disturbance in an FOG, in addition to shot noise. All the effects described in Table I generate phase noise that can affect the measurement of the angular velocity; because of this, in typical FOG configurations, mitigation strategies for all the sources of disturbance are implemented.

All the abovementioned techniques for noise reduction are implemented in the navigation-/strategic-grade FOGs, whose block diagram is shown in Fig. 4.

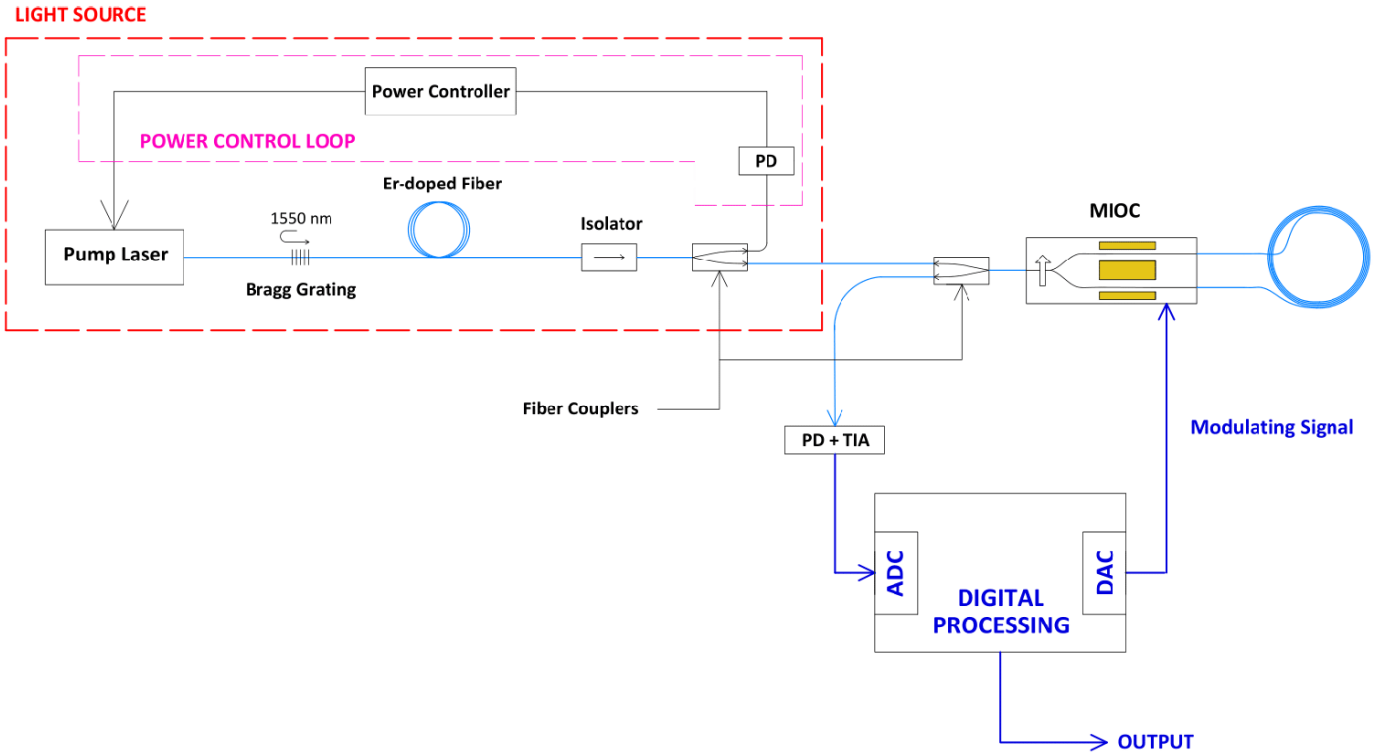

Fig. 4. Detailed FOG block diagram. PD: photodiode. TIA: transimpedance amplifier. ADC: analog-to-digital converter. DAC: digital-to-analog converter.

TABLE I
NOISE SOURCES AND COMMON MITIGATION APPROACHES IN FOG

NOISE SOURCE	DESCRIPTION	MITIGATION STRATEGIES
Polarization coupling noise	Birifrangence-induced effect that generates a spurious $\Delta\phi_R$ due to the interference between transmitted and and cross-polarization state components inside the ring interferometer	Coherence reduction between the spurious and main interference signals by using a PM fiber and a broadband source
Rayleigh backscattering	Loss mechanism due to local variation of the refractive index on a scale smaller than the optical wavelength λ. Randomly distributed defects generate back-reflections. The interference between back-reflected waves and the main waves generate a spurious $\Delta\phi_R$	Coherence reduction between forward and backward light waves using a broadband source and phase modulation to displace the noise outside the detection bandwidth
Shupe effect	Noise effect that generates parasitic $\Delta\phi_R$ due to the nonuniform distribution of temperature in the fiber coil	Special fiber coil fabrication techniques based on dipolar or quadrupolar symmetrical winding
Kerr effect	Nonlinear third-order effect induced by a high optical power density in an optical fiber core. The nonlinear variation of the refractive index induces a parasitic $\Delta\phi_R$ due to the interference between the counterpropagating waves	Coherence length reduction using a broadband source
Faraday effect	Effect induced by a longitudinal magnetic field that generates a circular birifrangence and a spurious $\Delta\phi_R$	Reduction of both the influence of the magnetic field by using a shield made of a high permeability material (μ-material), and the nonreciprocities induced by the birefringence by using a PM fiber
Broadband source central λ drift	Shift in the central λ of the emitting optical source due to fluctuations of the power supply, variations in temperature, and aging of the source. The drift introduces a parasitic $\Delta\phi_R$	Use of a broadband optical source with a more stable emission, such as a superluminescent source

C. Readout

In an interferometric FOG, a ring interferometer is used to detect the information of the phase difference between the two counterpropagating beams due to the Sagnac effect. The difference in phase is proportional to the rotation rate information. The signal that arrives at the photodetector is the response of the two-wave interferometer. The relationship between the optical power P and the phase shift $\Delta\phi$ between the two waves that interfere is expressed in the following equation:

$$P = \frac{P_0}{2}(1 + \cos(\Delta\phi)). \tag{6}$$

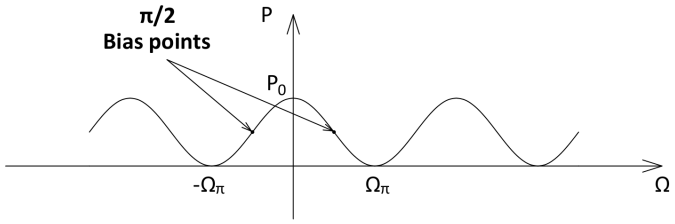

Fig. 5. Interference signal.

where P_0 is the optical power at the interferometer input. $\Delta\phi = \Delta\phi_R$ if no modulation is applied for the sensor readout.

The interferometric response is a cosine function of the two-wave phase difference induced by the rotation rate. The optical power is maximum at zero phase difference. The interference signal is shown in Fig. 5.

The sensitivity is given by (7); it is at the highest level when the phase difference is equal to $(\pi/2)$ and at the lowest level when the phase difference is approximately zero

$$\frac{\partial P}{\partial \Delta\phi} = \frac{P_0}{2}\sin(\Delta\phi). \tag{7}$$

To linearize the response and increase the sensitivity, several modulation techniques are used.

1) Open-Loop Configuration: To obtain higher sensitivity, the signal has to be skewed toward an operational point with a nonzero response slope. A phase bias angle ϕ_b is applied. A modulation electrical signal is applied to the phase modulator to avoid phase bias drift. A reciprocal phase modulator that acts as a retardation line is placed at the common port. The two interfering waves experience the same phase modulation but shifted in time. The delay is equal to the transit time τ defined as

$$\tau = \frac{nL}{c}. \tag{8}$$

As shown in (8), the transit time depends on fiber length L and the light velocity in the medium. The bias modulation of the phase difference between the two waves is expressed in the following equation:

$$\Delta\phi_m(t) = \phi_m(t) - \phi_m(t-\tau). \tag{9}$$

The response equation is given in the following equation:

$$P(\Delta\phi_R) = \frac{P_0}{2}(1+\cos(\Delta\phi_R + \Delta\phi_m)). \tag{10}$$

The modulation technique is implemented using a square wave with a period equal to 2τ and $\phi_m = (\phi_b/2)$ to create a total phase difference between the two counterpropagating waves equal to $\Delta\phi_m = \pm\phi_b$.

The signal is demodulated at the photodetector by using a lock-in amplifier. The demodulated signal is calculated through the difference between the even and odd power signals of the first and second semiperiods, τ. The difference signal at the photodetector is defined in the following equation:

$$\Delta P(\Delta\phi_R, \phi_b) = P_0 \sin(\phi_b)\sin(\Delta\phi_R). \tag{11}$$

The maximum sensitivity is obtained at $\Delta\phi_m = (\pi/2)$. Considering a $(\pi/2)$ square-wave bias modulation, $\Delta\phi_R$ is defined in the following equation:

$$\Delta\phi_R = \arcsin\left(\frac{\Delta P}{\sum P}\right). \tag{12}$$

where $\sum P$ is the summation of the even and odd power signals [33].

In an open-loop configuration, the angular rate measurement is based on an amplitude reading. The open-loop configuration measurements have low accuracy and sensitivity. To reach higher accuracy over the entire dynamic range and enhance the scale factor linearity, a closed-loop configuration is used.

2) Closed-Loop Configuration: The closed-loop configuration is useful for increasing the performance of the angular velocity sensor. In this configuration, a signal is used as feedback to control the sensor performance point at zero over the entire dynamic range. The feedback phase shift is nonreciprocal and compensates for the phase shift induced by the Sagnac effect so that the FOG works in a zero-crossing state [34].

As an error signal, the demodulated open-loop signal is sent back into the system to produce a second phase difference $\Delta\phi_{\mathrm{FB}}$ that is the exact opposite of the phase difference $\Delta\phi_R$ caused by rotation. In the closed-loop configuration, both the square-wave bias modulation signal and the feedback phase signal are applied at the modulator. The total phase difference between the two waves that interfere is given in the following equation:

$$\Delta\phi = \Delta\phi_R + \Delta\phi_{\mathrm{FB}} + \Delta\phi_m. \tag{13}$$

The measured value in the closed-loop configuration is $\Delta\phi_{\mathrm{FB}}$. The phase feedback value is independent of the returning optical power, so the stability of the response is increased. The interference signal depends only on the modulation phase shift ϕ_m because the rotation rate phase difference and feedback phase difference are servo controlled at zero.

The better approach for feedback signals is to apply a digital phase ramp. The phase ramp steps ϕ_S have a duration equal to the transit time through the coil τ. The induced phase difference $\Delta\phi_{\mathrm{FB}}$ is equal to ϕ_S.

Due to the limitations of the dynamic ranges of electrical components, a phase ramp signal with infinite steps cannot be produced. Digital phase ramp resetting is required and is implemented by overflow of the digital signal processing circuit. Since the interference signal has a periodicity of 2π, a 2π difference between the pre-reset and post-reset phase difference values is set. The resets are no longer periodic but are synchronized with τ and the biasing square wave. The detector signals for square-wave bias modulation and the closed-loop configuration are shown in Fig. 6.

In both cases, the detector signal contains spikes due to the square-wave bias modulation. In the closed-loop configuration, the detector signal is quite constant because of the zero-crossing modulation.

To achieve high compactness and high performance, the detection scheme of an FOG is implemented in an all-digital way. The implementation of the detection circuit using analog elements has many disadvantages in terms of poor repetition, difficulty in parameter adjustment, compensation

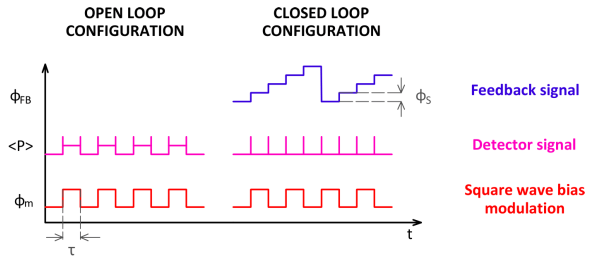

Fig. 6. Feedback signal, detector signal, and square-wave bias modulation for open- and closed-loop configurations.

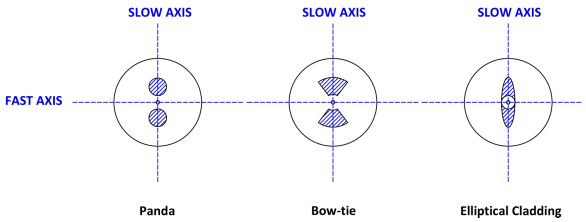

Fig. 7. Cross sections of the most commonly used high-birefringence PM fibers.

errors, parameter shifting with temperature, and a low dynamic range.

To reduce the costs, increase the speed, and increase the density of integration on a single device, a field-programmable gate array (FPGA) can be applied in the detection scheme, as reported, for example, in [34]. The FPGA is used for timing control, data collection, modulation and demodulation, square-wave generation, and digital ramp signal generation.

III. Miniaturization Strategies

The size and weight of interferometric optical gyroscopes basically depend on two aspects: 1) the external and internal diameters of the coil, which are influenced by the utilized optical fiber, and 2) the features, in particular the size, of the components and the electronic boards necessary for the generation of optical beams that counterpropagate in the coil and the readout of the sensor. This section critically examines the ways in which the coil and the optoelectronic system for beam generation and readout can be miniaturized. Interferometric gyroscopes based on waveguide coils that are integrated on a chip have recently been proposed. These are chip-scale miniaturized sensors whose main limitation is related to their obtainable performance, which is currently far from navigation grade. Such gyroscopes are discussed in Section III-C.

A. Coil Miniaturization

Typically, in an FOG, the coil consists of a single-mode PM optical fiber. As already mentioned, to mitigate the Shupe effect, the coil is wound according to a specific pattern, e.g., the quadrupole or octupole pattern. Several types of PM fibers, i.e., high-birefringence optical fibers specifically designed to maintain the polarization state of light propagating through them, have been reported in the literature, but the most commonly used are PANDA fibers, bowtie fibers, and elliptical cladding (tiger eye) fibers (see Fig. 7) [35]. In all these types, the polarization maintenance is stress-induced by using additional materials that have a thermal expansion coefficient approximately one order of magnitude larger than that of silica. Two highly doped silica rods, one on either side of the core region, are used to produce the fiber preform. These rods are often doped with boron, phosphorus, or aluminum. After pulling the fiber at a high temperature, these heavily doped rods will contract upon cooling, but their thermal contraction is prevented by the adjacent silica, which has a significantly lower thermal contraction. As a result, there is a compressive stress along the orthogonal axis and a tensile stress along the rod axis, both of which contribute to stress in the core region where light propagates. The PANDA fiber has circular rods; however, the bowtie fiber and elliptical cladding fiber both have a different form of the stressed region. In the bowtie fiber, the cross-sectional geometry resembles a bowtie, while in the elliptical cladding fiber, asymmetric stress on the core is created by the elliptical doped glass cladding, which results in stress-induced birefringence.

All three types of PM fibers mentioned above are available on the market, and the companies commercializing them are currently focusing their research and development efforts on minimizing the outer diameter of the PM fibers, aiming at developing thin-clad PM fibers [36]. Currently, several PM fibers intended for FOGs with cladding diameters of 60 or 80 μm and coating diameter in the range 100–200 μm are available on the market. Coils made with these fibers are also available. The experimental results in [36] clearly show that as the coating diameter decreases, the coil immunity to external stress is reduced, resulting in a higher potential for polarization cross-coupling in the fiber. For example, five different PM fibers with coating diameters ranging from 155 to 125 μm were experimentally studied in [36]. Each of the five fibers is coiled into a quadrupole FOG coil with an inner coil diameter $<$25 mm and a length $>$400 m. The polarization extinction ratio (PER) of the coil degrades by approximately 10 dB when the coating diameter is reduced from 155 to 125 μm. In addition, the PER change due to temperature drift is significantly larger for the fiber with a coating diameter $=$ 125 μm than for the fiber with a coating diameter $=$ 155 μm.

For the state-of-the-art, the minimum dimensions of the fiber coils specifically intended for FOG application (quadrupole or octupole winding pattern) are an internal diameter of 10–15 mm and an external diameter $<$30 mm [37]. Further research and development activities aimed at reducing the size of the coils made of standard PM fibers are currently ongoing, but a reduction in coil size inevitably implies a PER degradation that may not be compliant with the achievement of navigation grade. Thus, the target coil PER, which is strongly correlated with the target BIS, imposes a limit on coil miniaturization. This limitation is probably more stringent than that imposed by the bending loss that increases as the bending diameter decreases.

The reduction of the external diameter of the fiber coil inevitably needs the reduction of the external diameter of the fiber, generally speaking, less coating means less immunity to external stress, and, potentially, higher polarization cross-coupling in the fiber. Fiber coils made of PM fiber with

a coating diameter of 100 μm are on the market [38] and were utilized in miniaturized FOG prototypes [37], but a detailed characterization of these PM fibers is not available in the literature. At the state-of-the-art level, we do not have experimental evidence that these fibers and these coils with diameters <30 mm can support navigation-grade performance. Data in [37] only show that intermediate grade is achievable. A navigation-grade FOG integrating a coil with diameter = 40 mm and made of a standard PM fiber is on the market [39]. The research aimed at introducing new concepts for miniaturizing the FOG coil is currently focused on PM photonic crystal fibers (PCFs), potentially enabling a very small curvature radius, and multicore fibers (MCFs) that, in principle, could be used to reduce the overall coil volume; however, until now, no coil intended for FOGs having an external diameter <30 mm and based on the two technologies has been reported in the literature.

PCFs are a type of optical fiber that uses a 2-D periodic arrangement of dielectric materials to control and manipulate light propagation [40]. Unlike traditional optical fibers that have a solid-core surrounded by a cladding layer, PCFs have a microstructure design with an array of tiny air holes running through the entire length of the fiber. These air holes create a periodic pattern of the refractive index, forming a photonic crystal structure. The arrangement of the air holes determines the fiber optical properties and allows for unique light-guiding characteristics.

There are basically two distinct types of PCFs that differ in the way they guide and confine light within the fiber structure: solid- and hollow-core PCFs [41]. Solid-core PCFs have a microstructure design similar to that of traditional optical fibers but with the addition of a periodic arrangement of air holes surrounding the solid core. The solid core is typically made of a material with a higher refractive index, while the air holes introduce refractive index variations. The combination of the core and air-hole structures creates a photonic bandgap effect that confines light within the solid-state core. Hollow-core PCFs have a unique structure that consists of an air-filled hollow core surrounded by a cladding region composed of an array of air holes. The air holes are arranged to create a photonic bandgap structure that confines light within the core. PCFs have optical properties that are determined by their geometry, are made of only pure silica, and can guide light in air. Consequently, they possess some features that are potentially useful in the context of interferometric FOGs, including high immunity to radiation and other disturbances, e.g., temperature variations and magnetic fields, and extremely low nonlinearity (especially for hollow-core PCFs).

As already mentioned, fibers for FOG coils should be single mode, PM, and low loss. In addition, their bending loss should be very low. The PM solid-core PCF and the seven-cell hollow-core PCF have these features. A solid-core PCF with a four-ring air-hole structure specifically designed for FOGs was reported in [42]. The fiber has cladding and coating diameters of 100 and 135 μm, respectively. The attenuation at 1550 nm is approximately 2 dB/km. The coil with quadrupole winding pattern based on this fiber has an inner diameter of 26 mm and an outer diameter of 39 mm, approximately 10 mm larger than the state-of-the-art coils manufactured with standard PM fibers (see Fig. 8).

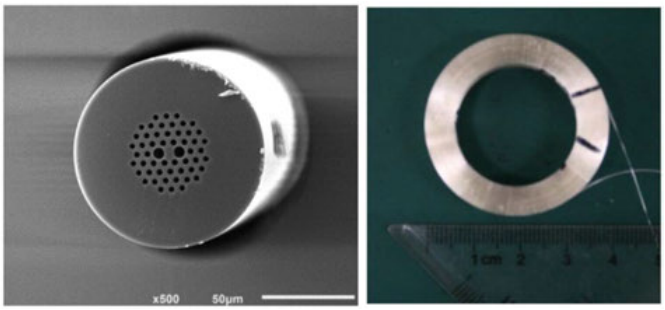

Fig. 8. On the left side, the solid-core PCF cross section, and on the right side the coil realized by solid-core PCF. © 2015 OPTICA. Reprinted with permission from [42].

Several prototypes of navigation-grade interferometric FOGs exploiting solid-core PCFs have been reported in the literature [43], [44]. The application of hollow-core PCFs in the FOG context has been numerically and experimentally studied since 2006 when the first prototype of an FOG whose coil had a diameter of 82 mm was made with a 235-m hollow-core PCF. The strong reduction of the Kerr, Shupe, and Faraday effects was experimentally proven despite the achieved performance being tactical grade. Other conceptually similar FOG prototypes were reported, achieving intermediate-grade performance [45].

A numerical study on a PM hollow-core PCF for FOGs was recently reported [46]. The bare fiber outer diameter was 80 μm. The simulations predict a propagation loss = 15 dB/km at 1550 nm, a birefringence of approximately 10^{-4}, and a negligible bending loss for a bending radius of 3 cm. No data on the bending loss for smaller radii were provided. The coil PER was not estimated.

MCFs are a type of optical fiber that contains multiple individual optical cores within a single fiber structure. The cores, which are typically arranged in a regular pattern, such as a square or hexagonal grid, can simultaneously carry independent optical signals. Such fibers have been developed for telecom applications, increasing the capacity for data transmission and saving space and cost, but they are also used in sensing. Recently, MCFs with a few tens of transmission cores were manufactured, and their viability was successfully tested in transmission experiments at the petabit/s scale [47].

The concept of an FOG integrating an MCF coil was envisaged approximately 15 years ago [9], but the first published experimental results are very recent. The basic idea is that the main part of the FOG, the fiber coil, can be made smaller overall by using an MCF without affecting the length of the optical path. This would be made possible by using multiple fiber cores rather than a single core to better use the volume of the fiber. The first prototype of interferometric FOG based on an MCF coil is reported in [48] and [49].

Fig. 9 shows the coil configuration, which incorporates a pair of fan-in/fan-out (FIFO) devices for slicing the MCF cores. Port n of the FI device is connected to port $(n-1)$

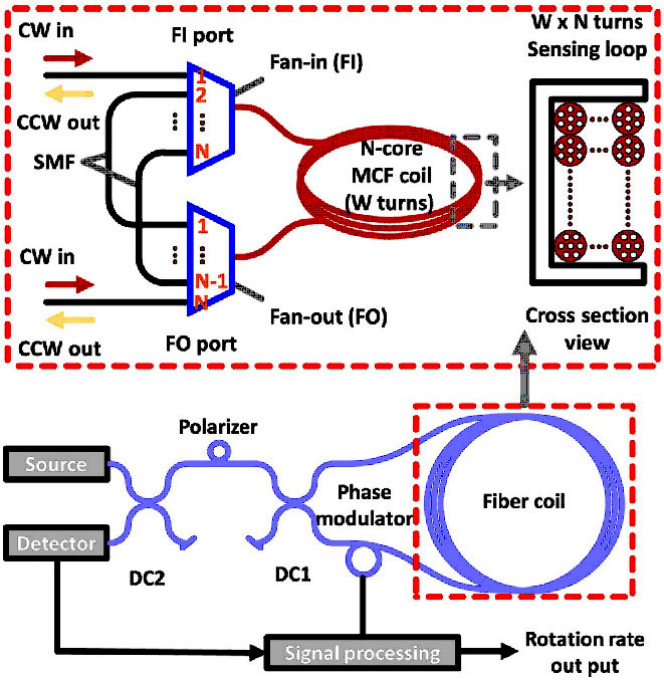

Fig. 9. FOG configuration using an MCF.

of the FO device ($n = 2, \ldots, N$). Port 1 of the FI device and port N of the FO device are connected to directional coupler DC1 via ports 1 and N, respectively [47].

The prototype is based on a coil made of a titanium bobbin with a diameter of 128 mm on which a 102.7-m-long MCF is wound using an octupole winding pattern. At a wavelength of 1550 nm, the loss of the wound MCF is 0.39 dB/km. The prototype also includes two FIFO devices built with free-space optics technology. The MCF coil and the FIFO devices were spliced. The whole optical path of the coil is 823.8 m. The BIS of this gyroscope is approximately 0.005 °/h.

Conceptually, similar MCF-based FOG prototypes having a coil with a slightly smaller diameter, down to 80 mm, have been reported in the literature. The achieved BIS is 0.01°/h [50].

Summing up, based on the theoretical and experimental studies reviewed in this section, we can state that: 1) the smaller fiber coils intended for FOG applications are still those made of the standard PM fibers (PANDA, bowtie, and tiger eye); 2) the minimum coating diameter for the standard PM fibers intended for FOG is 100 μm, enabling outer diameter values for the coil <30 mm, but the ability of such coils to support navigation-grade performance was never demonstrated; 3) a navigation-grade FOG integrating a coil with diameter = 40 mm is on the market; 4) PCF coils reported in the literature all have an outer diameter significantly larger than 30 mm, despite interesting advantages related to Kerr, Shupe, and Faraday effects mitigation that have been proved for hollow-core PCFs; and 5) some FOG prototypes using MCFs achieving navigation grade have been reported, but they include large fiber coils with an outer diameter of the order of 100 mm.

B. Broadband Optical Source: Available Options

As already mentioned, in all interferometric optical gyroscopes, the optical source is broadband to suppress several parasitic effects, such as the Kerr effect, Shupe effect, or Rayleigh backscattering. Such a source can be implemented using three basic approaches. All navigation-/strategic-grade FOGs on the market include a superfluorescent fiber source (SFS) with an erbium-doped (Er-doped) fiber, as shown in Fig. 4. This source shows a remarkable combination of high efficiency, great spatial coherence, broad spectrum emission, and outstanding long-term mean-wavelength stability. This last characteristic is essential since the scale factor stability of an FOG scales according to the stability of the mean wavelength of the source and precise measurement of the rotation rate requires accurate knowledge of the scale factor and the mean wavelength. The SFS is based on the amplified spontaneous emission from an Er-doped fiber optically pumped by a laser diode and can achieve a mean-wavelength stability of less than 1 ppm [51]. The configuration of the SFS [51], [52], which includes an Er-doped fiber coil with a typical length ranging from a few meters to tens of meters, a wavelength-division multiplexing coupler, a Faraday mirror or a Bragg fiber grating, and an isolator, makes miniaturizing the SFS to achieve a volume significantly below 100 cm^3 challenging. Some recent achievements in the field of photonic integrated circuit (PIC)-based Er-doped amplifiers [53] could trigger the development of next-generation chip-scale SFSs, but no evidence of the feasibility of such an optical source is available in the literature to our knowledge.

The most common alternative to the SFS is the superluminescent diode (SLD), which is a well-known edge-emitting semiconductor light source based on superluminescence. It combines the traditional low coherence of light-emitting diodes with the large power and brightness of laser diodes [54]. The SLD is a chip-scale optoelectronic component that is intrinsically miniaturized. It is available on the market in highly compact packages and, as will be discussed in Section III-C, can be integrated in complex PICs. Typically, for the SLD, the temperature drift of the mean wavelength is on the order of some hundreds of ppm/°C [55]; thus, regarding the state-of-the-art, SLD-based FOGs seem to be able to achieve only tactical/intermediate grades, while navigation/strategic grades demand more stable sources. A new approach for implementing a broadband optical source intended for navigation-/strategic-grade FOGs has been recently demonstrated [56], [57]. It is based on a narrow-linewidth standard laser diode whose output is frequency/phase modulated. An FOG with a linewidth-broadened laser meets the Federal Aviation Administration's Required Navigation Performance 10 criteria for aircraft navigation. An ARW of 0.0009 °/$\sqrt{\text{h}}$ and a BIS on the order of 0.01°/h have been reported [58]. This approach for implementing a broadband optical source seems promising for source integration on chip together with other FOG components. An accurate assessment of the scale factor stability of the laser-driven FOG seems necessary to fully evaluate the potential of this novel approach.

C. Miniaturization of the FOG Components via Integraed Microphotonics

A widely employed photonic integrated component in FOG systems is the $LiNbO_3$-based MIOC, which employs an optical power splitter to connect the input optical signal to a pair of electrooptic phase modulators for push–pull operation. The uniqueness of this MIOC includes a large second-order electrooptic coefficient and a high PER. The PER is typically larger than 60 dB to allow the suppression of the polarization crosstalk in the FOG system, thus minimizing the bias drift.

In recent years, researchers have aimed to miniaturize FOG systems by employing photonic integration technologies.

The basic idea of generic photonic integration technology is to support the monolithic and/or hybrid integration of precisely characterized photonic components that provide the basic functionalities required to realize a PIC. Two material systems, InGaAsP/InP and Si/silicon nitride (SiN)/SiO_2, have been widely explored for decades. Several foundries are now providing multiproject wafer (MPW) services for worldwide customers to implement PICs with lower fabrication barriers and shared costs. Leveraging photonic integration technologies in miniaturizing FOG components can greatly reduce the size, weight, cost, and power consumption while improving the shock and vibration robustness.

1) InGaAsP/InP-Based PICs for FOG Miniaturization: III–V material systems are well known for their tunable and direct bandgap characteristics at telecom wavelengths, and the epilayer structure can be optimized to realize SLDs and photodiodes, which serve as broadband light sources and photon detectors, respectively, in conventional FOG systems. However, a generic photonic integration platform is required for monolithic integration of multiple optical functionalities on a single chip.

Fig. 10 shows a schematic of the generic III–V photonic integration platform developed by an independent foundry, SMART Photonics [59]. Other institutes, such as Fraunhofer HHI, also provide III–V photonic integration platforms but with slightly different integration strategies [60]. Designers could implement a variety of active and passive photonic devices on this generic platform, such as semiconductor lasers, optical amplifiers, photodetectors, optical phase/amplitude modulators, and optical power splitters/combiners. This platform provides efficient light emission (>50 cm^{-1} optical modal gain), detection (>0.8 A/W responsivity), and phase modulation (~ 1.2 V·cm voltage–length product) functionalities. A broadband light source was developed by using a long optical amplifier section to generate amplified spontaneous emission and a loop mirror to enhance the optical power in the forward direction [61]. It generates a light source with 5 dBm output power, >20 nm bandwidth, and >21 dB PER at a wavelength of 1550 nm. Nevertheless, most active photonic devices are implemented on shallow-etched low-index-contrast (InGaAs as core material and InP as cladding material, $\Delta n \sim 0.2$) optical waveguides, so the waveguide bending radius should be larger than 400 μm to guarantee low-loss lightwave propagation. Even with a deeply etched waveguide geometry, the minimum bending radius is still 100 μm, which prevents dense photonic integration on InP.

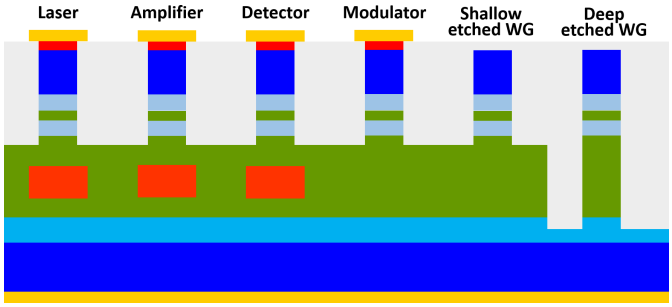

Fig. 10. Schematic of generic InP-based photonic integration platform.

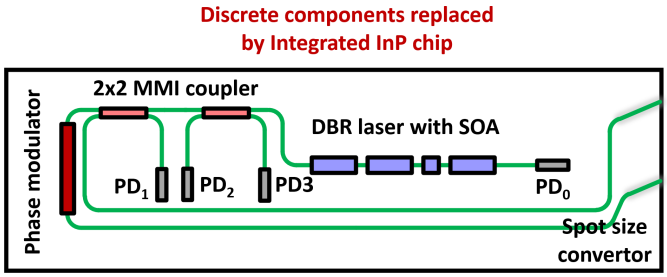

Fig. 11. Monolithic integration of active and passive FOG components except for the sensing coil through an InP photonic integration platform.

In addition, the fabrication processes for III–V photonic integration are not complementary metal–oxide–semiconductor (CMOS) compatible, and the wafer size is typically smaller than 6 in. This prevents the InP foundry from using an advanced deep-ultraviolet photolithography system dedicated to 8- or 12-in wafers.

Fig. 11 reveals an example of FOG component integration on InP, which comprises a distributed Bragg reflector laser with an integrated optical amplifier, an electrooptic phase modulator, three photodiodes, and a pair of optical power couplers [62]. This InP-based PIC, occupying an area of 6×2 mm, monolithically integrates all active and passive FOG components except for the sensing coil. A 5-km fiber coil is connected to this InP driver chip to form a Sagnac interferometer, and the intensity of the received signal is directly proportional to the angular rotation speed of the fiber coil. This example proves the feasibility of monolithic integration of FOG components on an InP generic platform but requires further consideration to make this approach promising. For example, there is no polarization filtering function on this chip to enable a high PER at the outputs of edge couplers, and the optical waveguide supports lightwave propagation for TE and TM polarizations. Several studies have focused on implementing a polarization beam splitter on InP, and most of them were based on the Mach–Zehnder interferometer (MZI) [63], [64], [65]. This device typically requires phase shifters on both arms of the MZI for fabrication error compensation to obtain the highest PER. In general, this device provides a PER of 20–30 dB over a broad wavelength range.

2) Si/SiN/SiO_2-Based PICs for FOG Miniaturization: Exploiting the well-established wafer-scale CMOS fabrication techniques, silicon photonics has shown remarkable large-scale photonic integration capabilities. The goal is to integrate several photonic functions on the same chip with low cost

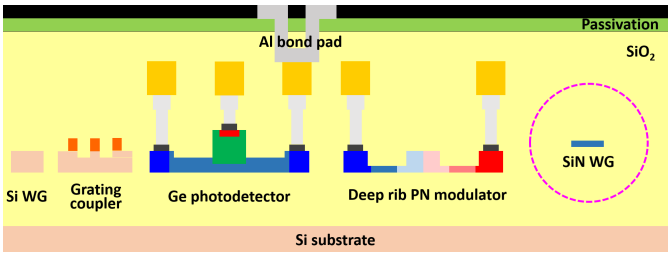

Fig. 12. Schematic of generic Si-based photonic integration platform.

and fingertip size using the generic PIC platform. After more than 20 years of development in both academia and industry, researchers and companies today can easily access this technology through a variety of service providers ranging from research institutes (such as IMEC, IHP, CORNERSTONE, and AIM Photonics) for prototyping to dedicated foundries (GlobalFoundries, TSMC, and TowerJazz) for volume production [66], [67], [68].

Fig. 12 shows a schematic of a generic Si-based photonic integration platform. Leveraging advanced deep-ultraviolet photolithography technology, the critical dimension (CD) of a silicon line can be as small as 130 nm or beyond. This allows designers to implement a variety of passive photonic components with fine features, such as surface grating couplers [69]. A silicon strip waveguide has a high refractive index contrast between the core and cladding material ($\Delta n \sim 2$), so it enables tiny waveguide dimensions (450 $\times$ 220 nm for single-mode propagation at a wavelength of 1550 nm) and a small bending radius (the extra loss for 10-μm waveguide bending is negligible). Therefore, silicon photonics allows a high photonic integration density with a small footprint. Designers could also implement active photonic devices such as germanium photodiodes and optical phase shifters on this generic photonic integration platform, but the light emission in silicon is quite inefficient.

The SiN waveguide is a low-index-contrast waveguide option ($\Delta n \sim 0.5$) available on this generic photonic integration platform. SiN waveguides have been included in Si-based photonic integration platforms to realize efficient edge couplers with mode matching to optical fibers.

An FOG was released in 2019 by leveraging an ultrathin (less than 100 nm) SiN waveguide in the PIC, as shown in Fig. 13. A light source in the short near-infrared 830-nm wavelength region is selected, which leads to a larger scale factor for the FOG system. This PIC consists of several passive FOG components, including a pair of low-loss optical power couplers, an optical polarizer, and mode size converters [70].

The optical polarizer comprises three 180° curved waveguides consecutively coupled to one another to form an "m" shape. This leads to very high propagation loss for TM-polarized light. Both the power splitter and polarizer enable a >45 dB PER, which is close to the PER provided by the $LiNbO_3$-based MIOC. As a result, this PIC not only polarizes the input light from the light source but also filters out the cross-coupled false signals in the return light from the sensing coil. However, in addition to the SiN PIC, it still requires a discrete light source, a photodetector, a piezoelectric

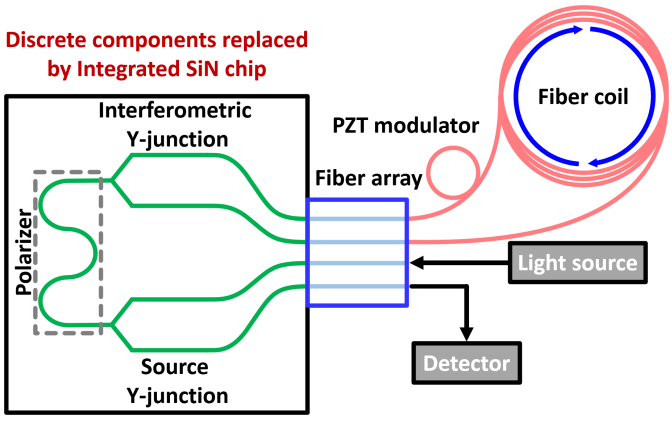

Fig. 13. Integration of passive FOG components through a SiN photonic integration platform while leaving active components and sensing coils off-chip.

transducer-based phase modulator, and a fiber coil to form the FOG that provides a BIS of 0.048 °/h.

Recently, active and passive FOG components except for the fiber coil and light source were monolithically integrated on a Si-based MIOC [71], [72]. Fig. 14 reveals the schematic and top view of the Si-based MIOC and its packaged module. The MIOC comprises a pair of electrooptic phase modulators, a Ge photodetector, a pair of 1 $\times$ 2 optical power couplers based on the multimode interference (MMI) principle, a waveguide polarization filter, a delay line, and a surface grating coupler array. The silicon phase modulator is based on carrier depletion of the silicon p-n junction formed in a silicon rib waveguide. The voltage–length product and modulation bandwidth of the phase modulator are approximately 1.97 V·cm and >10 GHz, respectively. Optical backscattering noise was suppressed by operating the phase modulator under the push–pull configuration. The optical field is strongly confined within the high-index-contrast silicon waveguide, so the electrooptic efficiency in silicon is almost ten times higher in the silicon phase modulator than in the bulk $LiNbO_3$-based MIOC. The Ge photodiode provides a responsivity of 1.05 A/W at a wavelength of 1550 nm. The overall chip dimensions are 4 $\times$ 1.2 mm, while the packaged module occupies a volume of 3.33 cm^3. Using grating couplers as optical input–output not only provides efficient optical coupling between the silicon photonic chip and optical PM fiber with wide alignment tolerance but also enables a high >40 dB fiber-to-fiber PER over wavelengths of 1500–1600 nm. The latter feature comes from the birefringence of the silicon waveguide, which makes light diffraction from the grating coupler at a specific wavelength efficient only for a single polarization according to the Bragg condition. The waveguide polarization filter is based on a bent waveguide directional coupler design that suppresses power exchange of TE-polarized light between waveguides. The resulting waveguide polarization filter provides >20 dB of extra PER in addition to the grating couplers. After connecting a fiber coil and a broadband light source to the silicon-based MIOC, the as-formed Sagnac interferometer provides tactical-grade gyroscope performance with ~0.1°/h BIS and ARW = 0.097 °/$\sqrt{\text{h}}$. The parasitic interface reflection originating from

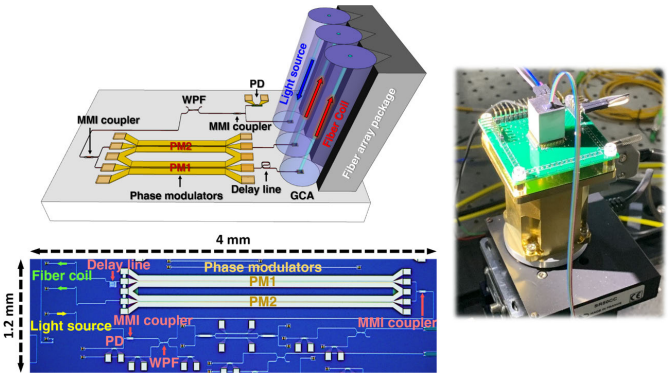

Fig. 14. Monolithic integration of active and passive FOG components except for the light source and sensing coil through a Si photonic integration platform. © IEEE. Reprinted with permission from [71].

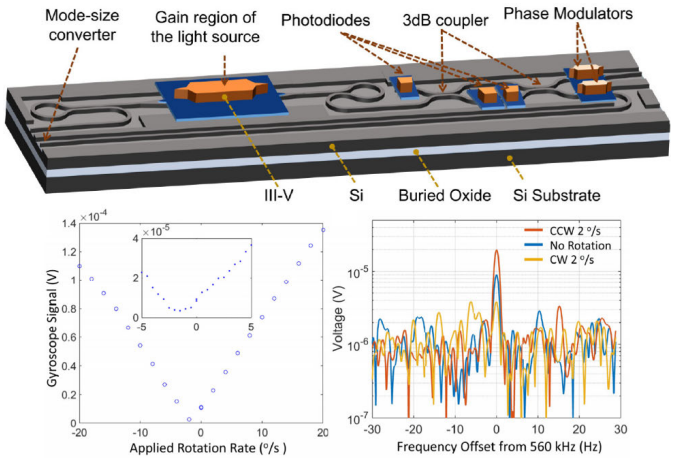

Fig. 15. Active FOG component integration through hybrid bonded III–V membranes on an SOI substrate where passive FOG components are implemented. The sensing coil is off-chip. © Optica. Reprinted with permission from [76].

the high-index-contrast silicon waveguide is still an unsolved issue for Si-based MIOCs. The interface reflection of a 1×2 silicon MMI power coupler is usually approximately -20 dB, which is high compared to that of a fiber-based directional coupler. This results in a degraded signal-to-noise ratio and a dc bias offset at the gyroscope output. Another parasitic interface reflection occurs at the grating couplers (approximately -18 dB) that form a parasitic Michelson interferometer. This also leads to a spurious bias voltage offset at the loop proper frequency, which is added to the Sagnac signal.

3) Heterogeneous III–V-on-Silicon PICs for FOG Miniaturization: The main idea behind silicon photonics is its potential to bring the mass-production capabilities of silicon fabrication to photonic components. The silicon-based photonic integration platform offers an almost complete suite of photonic components, including power splitters, polarization/wavelength filters, (de)multiplexers, modulators, and photodetectors. However, an efficient electrically pumped light source on silicon remains a challenge. Introducing III–V materials onto silicon to provide optical gain, detection, and modulation is a promising solution to this issue. One approach is to bond III–V dies on silicon with coarse alignment to the silicon waveguide and subsequently process them to realize the device structure [73], [74]. The advantages of this approach are the minimum requirement of expensive III–V materials and the possibility of integrating different epitaxial structures optimized for different functionalities or wavelengths. The bonding approach has been utilized to realize optical transceivers that are now available on the market. Another approach is to epitaxially grow III–V materials directly on silicon using intermediate buffer layer to minimize dislocations propagating into the active region [75].

The III–V-on-silicon photonic integration platform is promising for FOG miniaturization because it provides an optimized III–V epitaxial layer structure for light emission/detection and phase modulation. III–V active devices are optically interconnected by the underneath silicon waveguides where all passive devices are formed. Fig. 15 shows a schematic of an FOG driver chip based on a heterogeneous III–V-on-silicon platform and its FOG performance after connecting the chip to a fiber coil [76]. In this demonstration, a Fabry–Perot laser was formed as the light source by bonding the III–V gain material on top of a silicon resonant cavity formed by a pair of reflective loop mirrors. A pair of power splitters/combiners was also realized on silicon to construct a reciprocal FOG configuration. The III–V material for the photodiode shares the same epitaxial stacks with the gain material, and the resulting responsivity reaches 0.7 A/W. In contrast, the epitaxial stacks used for phase modulation are optimized to have a shallow band offset for the conduction band for more efficient carrier depletion [77]. The resulting phase modulator exhibits a voltage–length product of only 0.42 V·cm. The overall chip footprint is 0.5×9 mm. A Sagnac interferometer is formed by connecting this FOG driver chip to a PM fiber coil. The output signal voltage is linearly proportional to the applied rotation rate, but further FOG characterization, such as of the BIS, is missing.

Although FOG component integration on the III–V-on-silicon platform seems to be a promising solution, the chip design in Fig. 15 requires further optimization.

First, the Fabry–Perot laser should be replaced with a broadband SLD to eliminate the residual Rayleigh backscattering noise and nonreciprocal polarization coupling from the fiber coil. A broadband SLD was realized by hybrid bonding multiple InP dies on a silicon photonic circuit for the following quantum well intermixing process [78]. The resulting SLD enables a 3-dB bandwidth of 292 nm that covers the O, E, S, and C wavelength bands and an output power of -8 dBm. More recently, a heterogeneously integrated O-band SLD demonstrated continuous-wave light emission with 10-mW output power under the environment temperature of up to 65 °C [79].

Second, the FOG driver chip requires an extra polarization filtering function to achieve a high PER. The Si-based MIOC shown in Fig. 15 employs a bent waveguide directional coupler and grating couplers to provide an overall PER of >60 dB. The use of an advanced polarization filter design or cascading of multiple stages of a waveguide polarization filter could also increase the on-chip PER [80], [81].

D. Gyroscope-on-Chip Approaches

The sensing coils of the aforementioned photonic integrated FOGs are all based on optical fibers, in which the optical attenuation is less than 1 dB/km at telecom wavelengths. The length of the fiber coil, as the sensing element in an FOG system, is typically approximately 100–1000 m, and the diameter is usually on the order of a few centimeters. With the advent of integrated photonics suitable for wafer-scale processing, there is an opportunity to replace expensive and bulky fiber coils with smaller integrated photonic waveguide chips. The ultimate goal is to realize an all-chip-based FOG system either by monolithic or hybrid integration methodology. In this case, all FOG components can be manufactured using a wafer-scale fabrication process.

1) Waveguide Coil: Fig. 16 shows the cross-sectional view of low-loss waveguide geometries for InP-, silicon-on-insulator (SOI)-, SiN-, and silica-based photonic integration platforms. This figure also presents a schematic of a single-layer waveguide coil. Low-loss passive waveguides were demonstrated on InP [82], [83], and the waveguide loss increases during the fabrication due to active–passive monolithic integration. The typical waveguide loss for PICs fabricated by a generic InP foundry process is approximately 2–3 dB/cm. In recent studies, the waveguide loss was greatly reduced by restricting the p-dopant to active regions. With the help of localized Zn diffusion process, the waveguide loss was reduced to below 0.4 dB/cm for both TE- and TM-polarized light at the wavelength of 1550 nm. A waveguide coil realized on a semiconductor surface plane for an FOG system necessitates closely spaced waveguide crossings. This was achieved by excitation of a low-loss Bloch mode through superposition of the first- and second-order modes on an InP platform. As described in Section III-C, the main concern of InP-based PICs for FOG is the on-chip PER. Realizing an InP ridge waveguide that exhibits high birefringence for polarization maintenance and/or supports lightwave propagation for single polarization is quite challenging. The waveguide effective index difference for TE and TM polarizations is only 0.006, which leads to a long device length for polarization separation.

The physical dimensions of a silicon strip waveguide that supports single-mode propagation at a wavelength of 1550 nm are approximately 500 nm in width and 220 nm in height. The top and bottom interfaces of the silicon strip waveguide are atomically flat due to the high-quality SOI wafers. However, the photolithographically defined and etched waveguide sidewalls are not smooth. Sidewall roughness is the main source of propagation loss, especially in high-index-contrast silicon waveguides. The typical waveguide loss is approximately 1.5–2 dB/cm. The optical loss from sidewall roughness can be minimized by increasing the waveguide width. When the waveguide is widened to 2.5 μm, the propagation loss is marginally reduced to 1.3 dB/cm [84]. A silicon rib waveguide geometry, as opposed to a fully etched strip waveguide, was proposed to address this issue. A propagation loss as low as 2.7 dB/m has been shown to be achievable with a 200-nm rib on a 1-μm-thick silicon waveguide [85]. Recently, a shallow 56-nm rib on a 500-nm-thick SOI waveguide was fabricated to form a 52.2-cm-long spiral [86]. Although a silicon thickness of 220 nm is widely employed by silicon photonics foundries, the refractive index of a 500-nm-thick silicon layer is better matched to that of the III–V layer for mode hybridization [87]. A single-mode silicon rib waveguide (width = 1.8 μm) achieved a 16 dB/m propagation loss in the C-band. The loss was further reduced to 4 dB/m when the waveguide was widened to 8 μm. This is attributed to the lower optical field overlap with the etched rib sidewalls to minimize the light scattering. Weak optical confinement in a shallow silicon rib waveguide leads to a minimum bending radius of 800 μm. In comparison, a 70-nm etched silicon rib waveguide on 220-nm-thick SOI is available from most silicon photonics foundries. The typical waveguide loss at 1550 nm is approximately 0.5 dB/cm, and a bending radius of approximately 60 μm is required to ensure low-loss lightwave propagation.

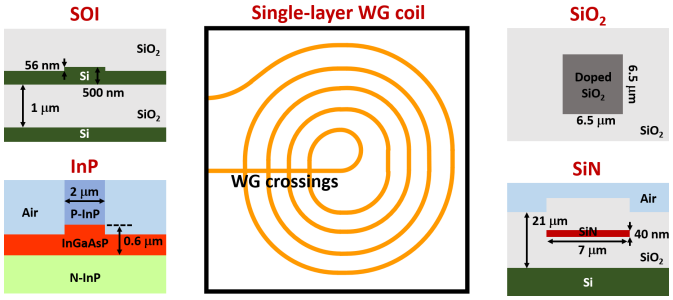

Fig. 16. Cross-sectional views of low-loss waveguide geometries made of different material systems, and schematic of a single-layer waveguide coil that contains closely packed optical crossings.

Employing low-index-contrast dielectric platforms, such as SiN or doped silica for ultralow-loss waveguide formation, is another promising approach. A SiN waveguide inherently has a tradeoff between the waveguide loss and the bending radius. A thinner waveguide core leads to reduced scattering loss, but its weak modal confinement leads to increased bending loss. This tradeoff ultimately leads to a thin but large waveguide coil, comparable to the size of a compact fiber coil. Nevertheless, similar to silicon rib waveguides, thin SiN-based waveguide coils are a CMOS-compatible solution that can enable ultralow propagation loss and high polarization-dependent loss. Moreover, the advantages of the SiN approach over silicon ribs include its low nonlinear loss and high nonlinear threshold. These unique characteristics play an important role in minimizing parasitic effects due to the optical Kerr effect. A 3-m-long waveguide coil made of a 40-nm-thick SiN waveguide exhibited a lightwave propagation loss of 0.78 dB/m and a PER of >75 dB [90], [91]. The upper and bottom cladding thicknesses should be larger than 5 μm to ensure minimum field overlap with the surface and silicon substrate. A waveguide spacing of 50 μm is needed to avoid mutual optical coupling among waveguides. The minimum bending radius of this waveguide coil is 17.25 mm, and its enclosed area is 278 cm^2. The area of this waveguide coil exceeds the space available in a reticle, so multiple separate masks exposed in succession are required to define the core. High-temperature (>1000 °C) annealing is also required to

TABLE II
COMPARISON OF WAVEGUIDE COILS MADE OF DIFFERENT MATERIALS AND THEIR FOG PERFORMANCE

WG Material	Physical Dimensions	Δn	Length (m)	Loss (dB/m)	Bend radius (μm)	ARW ($^\circ/\sqrt{h}$)	BIS ($^\circ$/h)	Ref.
InP	$w_{ridge} = 2$ µm $d_{core} = 600$ nm	0.196	0.06	30	> 1300	-	-	[82]
SOI	$w_{rib} = 8$ µm $d_{core} = 500$ nm	2.032	0.522	4	> 800	-	-	[86]
Si_3N_4	$w_{rib} = 7$ µm $d_{core} = 40$ nm	0.552	3	0.78	> 17250	8.5	58.7	[88]
Silica	$w_{core} = 6.5$ µm $d_{core} = 6.5$ m	0.006	2.14	3.91	> 30000	1.26	7.32	[89]

drive hydrogen contaminants out of the core and cladding layers to realize low material absorption loss. The thin SiN waveguide and large bending radius result in a low optical loss of only 0.015 dB/crossing at each crossing point. The packaged 3-m-long SiN waveguide coil exhibits an insertion loss of 16.2 dB, including fiber-chip coupling loss, and was placed in an FOG system with other discrete components to test its sensing characteristics. The high fiber-chip coupling loss is attributed to the mismatch between the modal size of the SiN waveguide and the butt-coupling fiber mode. The ARW and BIS were measured to be 8.52 $^\circ/\sqrt{h}$ and 58.7 °/h, respectively [91].

Silica-based photonic lightwave circuits have been widely developed to realize arrayed waveguide gratings for fiber optic communication applications. A large waveguide core and a low core/cladding refractive index contrast are the signatures of this waveguide platform, thus allowing efficient optical coupling between the silica waveguide and optical fiber. A silica waveguide with a core size of 6.5 × 6.5 μm and thick upper and lower claddings of 20 μm was fabricated to realize a 2.14-m-long spiral waveguide coil [89]. The silica core was doped with germanium to increase its refractive index by 0.006 compared to the surrounding cladding material. Such a low-index-contrast waveguide supports both TE- and TM-polarized lightwave propagation at a wavelength of 1550 nm and generates a symmetric field distribution with a modal field diameter of 8.17 μm. The minimum bending radius of the silica waveguide becomes 30 mm, which is not considered compact at all. Nevertheless, placing the silica waveguide coil in an FOG system for a sensing test resulted in an ARW of 1.26 $^\circ/\sqrt{h}$ and a BIS of 7.32 °/h.

We summarize the key parameters of four different waveguide platforms and their FOG sensing performance in Table II. The key design concept for ultralow-loss waveguides is to achieve weak optical confinement in the core. The InGaAsP/InP has a relatively low core/cladding index contrast Δn of 0.196, but material absorption limits the waveguide loss to 30 dB/m. The SOI waveguide system inherently has a very high Δn of 2.032 between silicon and silicon dioxide, but an expanded modal field diameter is achieved by employing a wide and shallow rib waveguide geometry that ultimately leads to a 4 dB/m loss. The SiN/SiO_2 waveguide provides a moderate Δn of 0.552. With an ultrathin and high-aspect-ratio waveguide geometry, the SiN waveguide tends to have weak optical confinement in the core, thus enabling a 0.78 dB/m propagation loss. The doped silica waveguide can be considered a "fiber-on-chip" solution because its Δn is only 0.006, which is comparable to the value of an SMF-28 optical fiber. The quoted loss of 3.91 dB/m includes the fiber-chip coupling loss; thus, the intrinsic waveguide loss should be even lower. The FOG performance revealed that the silica waveguide coil is a better solution than its SiN counterpart with a similar waveguide length in terms of the ARW and BIS. The very large bending radius of >30 mm required for a silica waveguide may limit its practical application in FOG systems because its enclosed area is even larger than that of a compact fiber coil.

The four waveguide coils discussed in Table II achieve a state-of-the-art propagation loss of a few dB/m, which is still three orders of magnitude higher than the loss of an optical fiber, hindering the ultimate FOG sensing performance. In addition to the waveguide loss, high Rayleigh backscattering and interface reflection at crossings also degrade the sensing performance when a waveguide coil is applied in an FOG system.

Fig. 17 shows the optical frequency-domain reflectometry (OFDR) traces of a 3.5-cm-long silicon slab waveguide coil with crossings and a 300-m-long PM fiber coil. The silicon waveguide coil was connected to an optical fiber through a pair of grating couplers, thus leading to strong reflection peaks at the input and output. For the single-layer waveguide coil, the output waveguide has to cross the turns of the waveguide coil, which results in many waveguide crossings. These crossings introduce additional loss, interface reflection, and optical crosstalk into the intersected waveguide, leading to degraded sensing performance. The actual OFDR traces of reported ultralow-loss waveguide coils should be better than

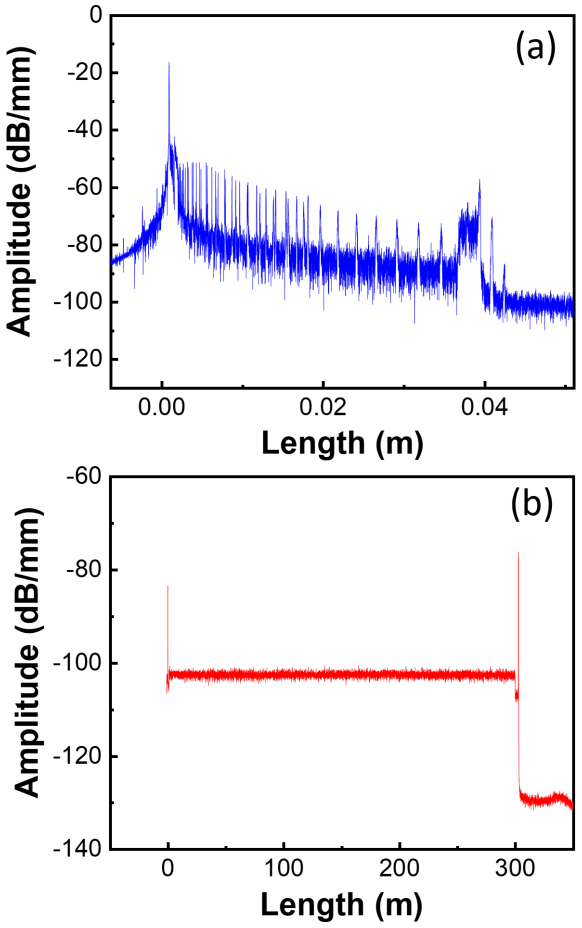

Fig. 17. Example of OFDR traces from (a) 3.5-cm-long silicon waveguide coil with crossings and (b) 300-m-long PM fiber coil.

the example in Fig. 17(a) in terms of the Rayleigh backscattering amplitude and interface reflection, and Fig. 17(b) may be the ultimate goal.

2) All Chip-Based Solution: There was no all-chip-based FOG solution in the literature or on the market until recently. ANELLO Photonics, a start-up company in CA, USA, disclosed their three-chip integration strategy (light source + silicon MIOC + SiN waveguide coil) in U.S. patents and presented it at major conferences [92], [93], [94]. Fig. 18 represents the schematics of their silicon MIOC and multilayer SiN waveguide coil. On the proposed silicon MIOC, they implemented three on-chip photodetectors in a reciprocal FOG configuration, and PD_1 is the main detector to receive the Sagnac signal. The other PD_2 and PD_3 provide in situ monitoring of optical fiber coupling between the light source and Si MIOC as well as the Si MIOC and SiN waveguide coil. This helps with chip-to-chip alignment and packaging. To avoid light leakage to the substrate, implants at a high dose were placed all the way through the slab around the waveguides that absorb scattered light. In general, an optical polarizer is needed between two power splitters to improve the on-chip PER value, but the need for a polarizer may be eliminated through proper design of the waveguide for TE-preferred lightwave propagation or the use of appropriate mode-selective

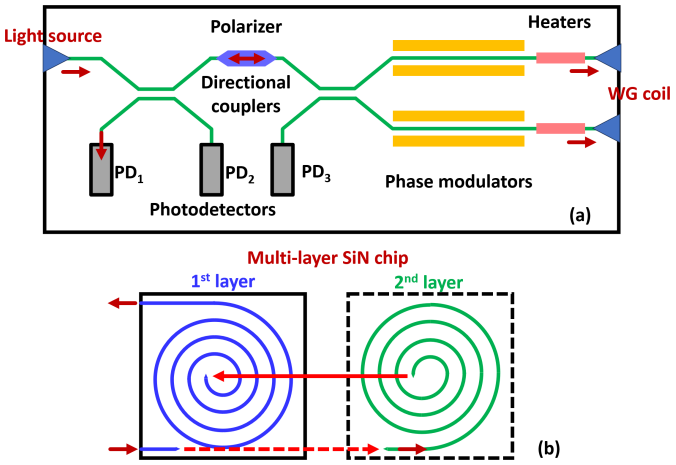

Fig. 18. Schematic of ANELLO Photonics' all-chip-based FOG solution: (a) silicon MIOC and (b) multilayer SiN coil.

filters. The resultant silicon MIOC occupies an area 2 × 5 mm and contains four power splitters, three photodetectors, two phase modulators, two thermo-optic heaters, one delay line, and one polarization filter. A low-loss SiN waveguide coil may be fabricated in a single layer, and the output waveguide has to cross the turns, which generates additional loss and interface reflection. As the sensing coil, the direction of light propagation has to remain the same within the coil. Fig. 18(b) shows the concept of a two-layer SiN waveguide coil, in which the output waveguide does not intersect with the turns of the waveguide coil. There are portions of the same waveguide coil on both the top plane and the bottom plane, and the output waveguide comes out from the same plane as the input waveguide for efficient coupling. In addition, by distributing the total length of the coil between two layers, the propagation length can be increased without increasing the footprint of the gyroscope coil. The 22-m-long SiN waveguide coil was fabricated by Tower Semiconductor based on dedicated process optimization, such as using chemical-mechanical polishing (CMP) to reduce the roughness of the top and bottom surfaces of the waveguide core. The ultimate waveguide loss reaches <0.5 dB/m and the Rayleigh backscattering amplitude is lower than −95 dB/mm. The silicon photonics-enabled chip-based FOG exhibits an ARW of 0.05 °/$\sqrt{\text{h}}$ and a BIS of 0.5 °/h (intermediate grade).

IV. Competitive Technologies

Many gyroscope technologies with different TRLs can compete with interferometric optical gyroscopes in terms of performance and SWaP budget. This article is on miniaturized gyroscopes, so we stay focused on the technologies that are already miniaturized, e.g., MEMS, or that can realistically enable IMUs with a volume of approximately 100 cm^3 and an SWaP product of the order of 10^{-5} $m^3 \cdot kg \cdot W$.

With reference to the technologies on the market, we consider the silicon-based MEMS gyroscope, RLG, and HRG. Basically, the former is the benchmark in terms of SWaP budget but now has limited applicability to the applications demanding navigation-grade performance. The latter two are

navigation and strategic grade but have an SWaP budget whose reduction without compromising performance is particularly challenging. Due to the substantial research effort on performance improvement of MEMS gyroscopes, in this section, we briefly review the main scientific achievements in the field of MEMS gyroscopes, especially because we believe that the research and development activity toward a navigation-grade MEMS gyroscope is currently competing with that aimed at miniaturizing interferometric optical gyroscopes while maintaining inertial-grade performance. Among the mid-TRL technologies that are not on the market, we mention the resonant FOG (RFOG), the chip-scale integrated photonic technologies based on active or passive integrated resonators, mainly the resonant micro-optical gyroscope (RMOG) and Brillouin gyroscope, and the nuclear magnetic resonance (NMR) gyroscope.

Since they will not be able to compete with miniaturized interferometric optical gyroscopes for many years, we do not consider low-TRL (<3) competing technologies such as the cold atom interferometer gyroscope and optical gyroscopes based on the emerging physical concept of exceptional points/surfaces. Despite the low TRL making any forecast of the success of these technologies complex, the former has very interesting prospects, especially in terms of miniaturization [95], due to the scale factor independence from the apparatus size, the performance already being comparable to that of interferometric FOGs, and some elements having reached the mid-TRL; the latter, according to a few recent papers, exhibits an improved responsivity that is precisely compensated by the increased laser noise [96].

A. Silicon-Based MEMS Gyroscopes

MEMS gyroscopes typically consist of a vibrating structure (proof mass) with two degrees of freedom. The mass can freely oscillate along two directions, also called the drive and sense mode directions. Due to the apparent Coriolis acceleration, oscillation in the drive mode direction, which is kept constant through electrostatic forces, leads to oscillation in the sense mode direction when the sensor is rotated around the axis orthogonal to both the drive and sense mode directions. This gyroscope is on the market, TRL = 9.

The sensor can be operated in either mode-matched or split-mode conditions, depending on whether the drive and sense modes are matched or intentionally mismatched in frequency. Generally, mode-matched sensors have better performance than split-mode sensors, but they exhibit a narrower bandwidth and higher power consumption, requiring more complex electronics to guarantee matching stability over temperature and time. Regarding the state-of-the-art, the best-performing prototypes of MEMS gyroscopes are mode-matched disk resonating gyroscopes with a BIS slightly less than 0.01°/h, measured at room temperature [97], [98]. A dual mass mode-matched MEMS gyroscope with special encapsulation achieving a BIS <0.03 °/h was reported in [99].

The technology of split-mode MEMS gyroscopes is quickly advancing. A performance that is quite similar to that demonstrated for mode-matched gyroscopes has been recently achieved by split-mode sensors with temperature-compensated output, whose main advantage is the lower power consumption. In particular, the prototype MEMS gyroscope reported in [100], which has a tuning fork configuration, exhibits a BIS of 0.01°/h (at constant temperature), with a bandwidth >300 Hz. A split-mode MEMS gyroscope with nanoresistive sensing was recently demonstrated with a BIS of 0.02°/h (under an uncontrolled laboratory environment with maximum temperature variations during measurements of ±2 °C) [101]. These prototypes of navigation-grade or near-navigation-grade MEMS gyroscopes are still quite far from commercialization, and their control and readout electronics are often based on board-level circuits formed by sophisticated digital processors and ultralow noise analog components, with an interesting exception being the system formed by an integrated circuit and a micromachined piezoresistive gyroscope reported in [101].

Currently, the best-performing MEMS gyroscopes on the market have a BIS on the order of 0.1°/h (intermediate grade), one order of magnitude worse than that of the mid-TRL high-performance prototypes reported in the last decade and reviewed in this section.

MEMS gyroscopes are intrinsically based on moving parts, which may make their use in harsh environments potentially critical, for example, in space missions. To our knowledge, no space-qualified silicon MEMS gyroscope is available on the market. The European Space Agency funded the development of a MEMS gyroscope (SiREUS) for space applications, but its qualification highlights some critical aspects mainly related to mechanical shocks and random vibrations [102].

B. Resonant Photonic Gyroscopes

Optical resonators with a high Q-factor and high finesse can be used to sense rotation, exploiting the Sagnac effect. The only gyroscope based on this principle that has reached the commercialization stage is the He–Ne RLG, which is based on a bulk-optics lasing cavity made of three or four mirrors, where light propagates in a He–Ne gas mixture [103]. Within the ring laser cavity, two counterpropagating beams are generated. The interference of the two beams generates a beating signal whose frequency is directly proportional to the angular rate. The He–Ne RLG is a navigation-grade sensor widely used in the aerospace and defense markets. Its miniaturization without performance degradation is challenging.

A miniaturized gyroscope based on the same general concept as the He–Ne RLG is the chip-scale Brillouin laser gyroscope [104] having a TRL equal to 3–4. The sensor is based on a silica wedge resonator (loaded Q-factor >100 million) with a diameter of 36 mm, which is an optically pumped lasing cavity (see Fig. 19). The cavity is optically pumped by two counterpropagating pump beams to generate counterpropagating, narrow-linewidth Brillouin lasers. The laser-generated beams interfere, thus generating the beating signal, which has a frequency directly proportional to the angular rate. The gyroscope is tactical grade with a BIS of 3.6 °/h.

Passive optical cavities supporting two counterpropagating resonant modes excited by a laser source external to the cavity can also be used to sense rotation. The practical implementation of such sensors can be achieved by using either fiber ring resonators or chip-scale ring resonators. The gyroscopes based

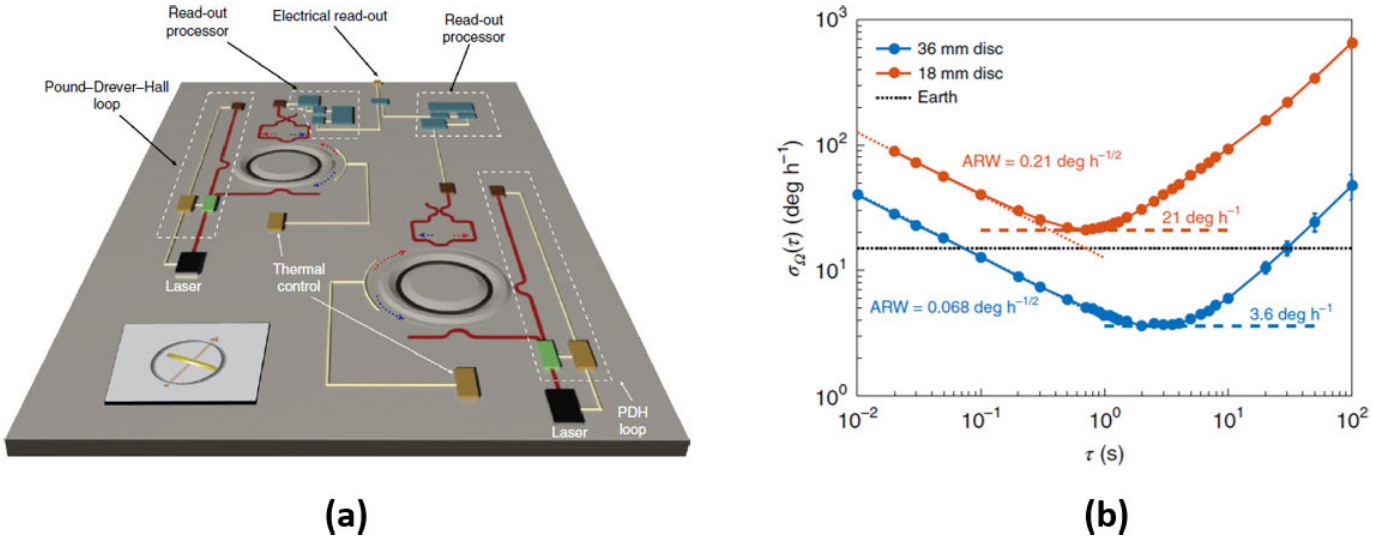

Fig. 19. (a) Chip-scale Brillouin laser gyroscope scheme. (b) Allan deviation evaluated graph. © 2020 Springer Nature Group. Reprinted with permission from [104].

on the former cavities are called RFOGs, while the sensors based on the latter cavities are called RMOGs. In principle, an RFOG is capable of reaching the same performance as the interferometric FOG with much less optical fiber due to the recirculation of light in the resonant cavity. In practice, RFOGs have been investigated for many years but have never reached the market because their miniaturization is challenging and they need a complex optoelectronic system for cavity excitation and readout. A near-navigation-grade RFOG with a BIS of 0.02 °/h, which was based on a fiber ring resonator with a diameter of 50.8 mm and a fiber length of 100 m, was reported in [105]. The gyroscope readout is obtained by a complex modulation technique that requires many sophisticated optoelectronic components.

Very recently, RFOGs with fiber ring resonators with a diameter <75 mm reached navigation grade [106], [107]. The sensors do not use a narrow-linewidth laser beam for cavity excitation but a broadband laser source. The achieved BIS is slightly less than 0.01°/h. Despite the important scientific value of such results, the RFOG excited by a broadband light source still has no evident advantages with respect to the standard interferometric FOG, except for the shorter length of the fiber utilized for the sensor implementation. In addition, in RFOGs, the reduction of the diameter of the fiber ring resonator is probably critical because it has a direct negative impact on the finesse and Q-factor of the cavity, with consequent degradation of the performance. Navigation-grade interferometric FOGs with a coil diameter of 40 mm are already on the market [108], while demonstrating a navigation-grade RFOG based on a fiber ring resonator with the same diameter seems challenging. Additional details on the RFOG technology, having a TRL equal to 4–5, are available in [109].

RMOGs have been widely investigated in recent decades, aiming at demonstrating miniaturized chip-scale gyroscopes based on integrated microphotonics. The RMOG is conceptually similar to the RFOG, but its sensing element is a miniaturized optical cavity typically manufactured on chip using a low-loss waveguide structure. Thus, the RMOG is an intrinsically miniaturized gyroscope with an SWaP budget comparable to that of MEMS sensors. Regarding the state-of-the-art, the best RMOG prototypes, which do not include moving parts, are tactical grade. A bias stability of 3 °/h has been obtained in an RMOG whose sensing element is a whispering gallery mode CaF_2 optical cavity with a diameter of 7 mm and a finesse of 100 000 [110]. Some physical limitations of the RMOG are highlighted in [111] and [112]. The TRL of the RMOG technology is 3–4.

C. NMR Gyroscopes

The quantum spin of atomic nuclei is used by an NMR gyroscope to detect rotation [113]. The spin vector of an atom precesses around a magnetic field B_0, at the Larmor frequency, $\omega_L = \gamma B_0$, where γ is the gyromagnetic ratio and depends on the atomic species. The rotation rate Ω increases the observed precession frequency $\omega_I = \omega_L + \Omega$ if the frame is rotated around B_0 [114]. This physical effect can be utilized in the context of gyroscope technologies. In a microfabricated vapor cell, the NMR gyroscope utilizes a large number of multiple species of atoms, including alkali and noble gas atoms. The atomic mixture is illuminated by a circularly polarized optical beam aligned with B_0. The beam is generated by a pump laser and is in resonance with an alkali atomic optical transition. As a consequence, the atomic spin of the alkali atoms is aligned. During collisions between noble gas and alkali atoms, the polarization of the alkali atoms is transferred to the noble gas nuclei. Noble gas atoms precess about the applied magnetic field at the Larmor frequency, but they are arbitrarily phased despite precessing at the same rate. The spin precession of noble gas atoms is brought into coherent motion by applying additional ac magnetic fields perpendicular to B_0. Due to the fact that the alkali atoms precess around the combination of B_0 and the magnetic field caused by the noble gas atoms, the noble gas precession can be measured by observing the alkali atoms. The polarization of alkali atoms

is measured using a probe beam that is orthogonal to the pump beam. Since the sensitivity of the NMR gyroscope does not scale with size, unlike optical and Coriolis gyroscopes, it is theoretically possible to develop small-volume, high-performance sensors. In addition, the sensing mechanism is inherently vibration-resistant. The first prototype of a compact NMR gyroscope with a volume of only 10 cm^3 and a BIS of 0.02 °/h was demonstrated approximately ten years ago [115]. This sensor is based on a millimeter-scale alkali/noble gas vapor cell filled using conventional glass-blowing techniques. The MEMS atomic vapor cell for gyroscope applications was demonstrated [116], aimed at enhancing the TRL, making this technology competitive with mature technologies. The current TRL of the NMR gyroscope is 3–4.

Low-TRL (<3) prototypes of a new class of nuclear spin gyroscopes, conceptually analogous to vapor-based NMR devices, have been recently reported. These sensors are based on nitrogen-vacancy color centers in diamond [117], [118], [119], [120].

V. Conclusion

Miniaturization is a fundamental technological driver, and its application to very successful optoelectronic sensors, such as the FOG, has been reviewed in this article. Miniaturized navigation-grade FOGs that can be integrated into IMUs with a volume smaller than 100 cm^3 do not exist on the market and have never been experimentally demonstrated.

The most difficult component of the FOG to miniaturize is the coil. If it is made of fiber, then its minimum external diameter for navigation-grade performance is approximately some tens of millimeters, which is not fully compatible with demonstrating a miniature navigation-grade FOG. If the coil is implemented on chip using a planar waveguide, then its maximum length is currently on the order of a few meters, which is not compliant with the navigation-grade performance class. Overcoming the current limitations mentioned above is the aim of various research activities underway worldwide, the success of which appears uncertain. In the field of miniaturization of the broadband optical source, important results have been recently achieved, including the implementation of the source using a laser diode with phase-modulated output. These findings will have a significant impact on the miniaturization of FOGs once additional experimental evidence backs them up. In principle, the remaining optical and optoelectronic components of the FOG, as well as the source, can be integrated into a single chip. The various attempts made in this direction show that the achievement of a PER of 60 dB, which is typical for a $LiNbO_3$ MIOC, is challenging. Source integration is relatively simple only for an SLD, whose stability is typically considered to be not compliant with navigation grade.

Recently, quick technological progress in the concept of an interferometric optical gyroscope fully integrated on a silicon chip has been made. Moreover, the combination of a photonic integrated FOG for high-performance and MEMS-based IMUs for roll and pitch information as well as three-degree-of-freedom accelerometers through a sensor fusion engine is considered a competitive navigation solution in terms of performance, SWaP budget, and cost compared to pure FOG- and MEMS-based IMUs [121]. This innovative approach is intended for several applications that do not demand navigation grade and have large potential markets, such as self-driving vehicles and robots.

In summary, we believe that integrated microphotonics is mature enough to allow the demonstration of a miniaturized navigation-grade FOG in the medium term. This result should have a clear scientific value, but it can only be reached with large investments from both the public and private sectors. These investments are likely to occur only if the advantages over the main competing technology, i.e., silicon-based MEMS gyroscopes, are clear. MEMS gyroscope technology is rapidly advancing, and the possibility that in the short-to-medium term, it will simultaneously reach the navigation-grade performance class and levels of immunity to disturbances compatible with the requirements imposed by the main emerging applications, which often demand both miniaturization and high performance, cannot be excluded.

References

[1] A. Lawrence, *Modern Inertial Technology: Navigation, Guidance, and Control*, 2nd ed. New York, NY, USA: Springer, 1998.

[2] D. H. Titterton and J. L. Weston, *Strapdown Inertial Navigation Technology*, no. 17, 2nd ed. Stevenage, U.K.: The Institution of Engineering and Technology, 2009.

[3] V. Apostolyuk, *Coriolis Vibratory Gyroscopes: Theory and Design*, 1st ed. Cham, Switzerland: Springer, 2016.

[4] E. J. Post, "The Sagnac effect is a phenomenon in which a change in the orientation of an interferometer causes a shift in the interference pattern," *Rev. Modern Phys.*, vol. 39, no. 2, pp. 475–493, Apr. 1967.

[5] G. Zhanshe, C. Fucheng, L. Boyu, C. Le, L. Chao, and S. Ke, "Research development of silicon MEMS gyroscopes: A review," *Microsyst. Technol.*, vol. 21, no. 10, pp. 2053–2066, Oct. 2015.

[6] E. J. J. Loper and D. D. Lynch, "Vibratory rotation sensor," U.S. Patent 4 951 508, Aug. 8, 1990.

[7] A. Torasso, R. Diram, and S. Kowaltschek, "Design and test results of a rad tolerant space qualified CVG," in *Proc. DGON Inertial Sensors Syst. (ISS)*, Braunschweig, Germany, Sep. 2022, pp. 01–16.

[8] G. Remillieux and F. Delhaye, "Sagem coriolis vibrating gyros: A vision realized," in *Proc. DGON Inertial Sensors Syst. (ISS)*, Karlsruhe, Germany, Sep. 2014, pp. 1–13.

[9] R. Bergh, H. Lefevre, and H. Shaw, "An overview of fiber-optic gyroscopes," *J. Lightw. Technol.*, vol. 2, no. 2, pp. 91–107, Apr. 1984.

[10] W. W. Chow, J. Gea-Banacloche, L. M. Pedrotti, V. E. Sanders, W. Schleich, and M. O. Scully, "The ring laser gyro," *Rev. Mod. Phys.*, vol. 57, no. 1, pp. 61–104, Jan. 1985.

[11] *STIM300 Datasheet*. Accessed: Aug. 30, 2023. [Online]. Available: https://sensonor.azurewebsites.net/media/1132/ts1524r9-datasheet-stim300.pdf

[12] *HG4930 Datasheet*. Accessed: Aug. 30, 2023. [Online]. Available: https://aerospace.honeywell.com/content/dam/aerobt/en/documents/learn/products/sensors/brochures/N61-1523-000-010-HG4930-MEMS-Inertial-Measurement-Unit-bro.pdf

[13] *DMU41 Datasheet*. Accessed: Aug. 30, 2023. https://www.siliconsensing.com/media/31186/dmu41-00-0100-131-rev-3.pdf

[14] *KVH 1750 Datasheet*. Accessed: Aug. 30, 2023. [Online]. Available: https://www.canalgeomatics.com/wp-content/uploads/2019/11/kvh-1750-imu-datasheet.pdf

[15] *UmiX U9 Datasheet*. Accessed: Aug. 30, 2023. [Online]. Available: https://www.ixblue.com/wp-content/uploads/2021/12/datasheetumix-u9.pdf

[16] *LN 200 Family Datasheet*. Accessed: Aug. 30, 2023. [Online]. Available: https://www.northropgrumman.com/wp-content/uploads/LN-200-FOG-Family-datasheet.pdf

[17] *HG9900 Datasheet*. Accessed: Aug. 30, 2023. [Online]. Available: https://aerospace.honeywell.com/content/dam/aerobt/en/documents/learn/products/sensors/brochures/N61-1638-000-000-hg9900inertialmeasurementunit-bro.pdf

[18] *D90 Datasheet*. Accessed: Aug. 30, 2023. [Online]. Available: https://www.advancednavigation.com/wp-content/uploads/2021/08/Boreas-D90-Datasheet.pdf

[19] *Astrix 1120 Datasheet*. Accessed: Aug. 30, 2023. [Online]. Available: https://www.ixblue.com/wp-content/uploads/2021/12/datasheetastrix90.pdf

[20] *Triton IMU-Strategic Grade Datasheet*. Accessed: Aug. 30, 2023. [Online]. Available: https://static1.squarespace.com/static/5508321ae4b0957561314185/t/62e6c8f2dd9c662e313be885/1659291890942/2022_Triton_Strategic-Grade_Brochure_.pdf

[21] *SIRU-E Datasheet*. Accessed: Aug. 30, 2023. [Online]. Available: https://www.northropgrumman.com/wp-content/uploads/Scalable-SIRU-family-of-products-brochure.pdf

[22] *Astrix 200 Datasheet*. Accessed: Aug. 30, 2023. [Online]. Available: https://www.ixblue.com/wp-content/uploads/2021/12/datasheetastrix200.pdf

[23] *Black-Onyx Datasheet*. Accessed: Aug. 30, 2023. [Online]. Available: https://safran-navigation-timing.com/wp-content/uploads/2023/02/Safran-Electronics-Defense-NAVAL-NAVIGATION-SYSTEMS-1.pdf

[24] G. E. Moore, "Cramming more components onto integrated circuits," *Proc. IEEE*, vol. 86, no. 1, pp. 82–85, Jan. 1998.

[25] J.-D. Emerard et al., "Si-MEMS gyro by Safran: Towards the navigation grade," in *Proc. IEEE Int. Symp. Inertial Sensors Syst. (INERTIAL)*, Avignon, France, May 2022, pp. 1–4.

[26] A. Buffoli, P. Segala, M. Gadola, T. Verdot, P. Robert, and G. Langfelder, "Searching for the origin of zero-rate offset and scale-factor drift in NEMS-based Nav-grade gyroscope," in *Proc. IEEE Int. Symp. Inertial Sensors Syst. (INERTIAL)*, Lihue, HI, USA, Mar. 2023, pp. 1–4.

[27] I. P. Prikhodko, B. Bearss, C. Merritt, J. Bergeron, and C. Blackmer, "Towards self-navigating cars using MEMS IMU: Challenges and opportunities," in *Proc. IEEE Int. Symp. Inertial Sensors Syst. (INERTIAL)*, Mar. 2018, pp. 1–4.

[28] L. Blocher et al., "Gyroscope-aided odometry navigation using a highly-precise automotive MEMS IMU complemented by a low-cost sensor array," in *Proc. IEEE Int. Symp. Inertial Sensors Syst. (INERTIAL)*, France, May 2022, pp. 1–4.

[29] S. Donati, *Photonic Instrumentation: Sensing and Measuring With Lasers*. Boca Raton, FL, USA: CRC Press, 2023.

[30] G. Sagnac, "L'éther lumineux démontré par l'effet du vent relatif d'éther dans un interféromètre en rotation uniforme," *C. R. Acad. Sci.*, vol. 157, pp. 708–710, 1913.

[31] H. Lefèvre, *The Fiber-Optic Gyroscope*, 3rd ed. London, U.K.: Artech House, 2022.

[32] X.-L. Zhang, H.-L. Ma, Z.-H. Jin, and C. Ding, "Open-loop operation experiments in a resonator fiber-optic gyro using the phase modulation spectroscopy technique," *Appl. Opt.*, vol. 45, no. 31, p. 7961, Nov. 2006.

[33] S. Öğüt, 'Implementation of digital detection scheme for fiber optic gyroscope," Ph.D. thesis, Dept. Elect. Electron. Eng., Bilkent Univ., Bilkent, Turkey, 2013.

[34] J. Han, "Implementation of digital detection scheme for closed-loop FOG based on DSP and FPGA," in *IEEE Instrum. Meas. Technol. Conf.*, Dec. 2006, pp. 2221–2225.

[35] J. Noda, K. Okamoto, and Y. Sasaki, "Polarization-maintaining fibers and their applications," *J. Lightw. Technol.*, vol. 4, no. 8, pp. 1071–1089, Aug. 1986.

[36] A. Gillooly and M. Hill, "HiBi fiber design considerations for polarization maintaining fiber optic gyroscopes (FOG)," in *Proc. DGON Inertial Sensors Syst. (ISS)*, Sep. 2021, pp. 1–11.

[37] K. Shang et al., "Ultra-small interferometric fiber optic gyroscope with an integrated optical chip," *Chin. Opt. Lett.*, vol. 20, no. 4, 2022, Art. no. 040601.

[38] *Panda PMF Specifications*. Accessed: Oct. 17, 2023. [Online]. Available: https://www.yoecgroup.com/specialty-optical-fibers/polarizing-fibers/PM-fibers.html

[39] E. de Toldi et al., "ASTRIX NS: A small, accurate, versatile and cost-efficient fiber optic gyroscope," in *Proc. 4S Symp.*, Vilamoura, Portugal, May 2022, pp. 1–10.

[40] J. C. Knight, "Photonic crystal fibres," *Nature*, vol. 424, pp. 847–851, Aug. 2003.

[41] F. Poli, A. Cucinotta, and S. Selleri, *Photonic Crystal Fibers: Properties and Applications*. Dordrecht, The Netherlands: Springer, 2007.

[42] N. Song, W. Cai, J. Song, J. Jin, and C. Wu, "Structure optimization of small-diameter polarization-maintaining photonic crystal fiber for mini coil of spaceborne miniature fiber-optic gyroscope," *Appl. Opt.*, vol. 54, no. 33, pp. 9831–9838, Nov. 2015.

[43] N. Song, X. Xu, Z. Zhang, F. Gao, and X. Wang, "Advanced interferometric fiber optic gyroscope for inertial sensing: A review," *J. Lightw. Technol.*, vol. 41, no. 13, pp. 1–14, Jul. 2023.

[44] M. Li, X. Zhao, F. Hui, J. Liu, F. Li, and B. Liu, "Optimized design on polarization maintaining photonic crystal fiber for higher precision FOGs," in *Proc. IEEE Int. Symp. Inertial Sensors Syst. (INERTIAL)*, Hiroshima, Japan, Mar. 2020, pp. 1–5.

[45] X. Xu, N. Song, Z. Zhang, and J. Jin, "Backward secondary-wave coherence errors in photonic bandgap fiber optic gyroscopes," *Sensors*, vol. 16, no. 6, p. 851, Jun. 2016.

[46] H. Cai et al., "Thin-diameter polarization maintaining hollow-core photonic bandgap fiber for fiber optic gyroscope," *Opt. Fiber Technol.*, vol. 55, Mar. 2020, Art. no. 102141.

[47] G. Rademacher, R. S. Luís, B. J. Puttnam, Y. Awaji, and H. Furukawa, "Petabit-per-second class transmission and switching," in *Proc. 27th OptoElectron. Commun. Conf. (OECC) Int. Conf. Photon. Switching Comput. (PSC)*, Toyama, Japan, Jul. 2022, pp. 1–3.

[48] S. Mitani, K. Nigo, S. Karasawa, Y. Tottori, H. Ehdo, and T. Takahata, "Interferometric fiber-optic gyroscope using multi-core fiber," in *Proc. Eur. Conf. Opt. Commun. (ECOC)*, Rome, Italy, Sep. 2018, pp. 1–3.

[49] S. Mitani et al., "Interferometric fiber-optic gyroscope using multi-core fiber," *J. Lightw. Technol.*, vol. 37, no. 21, pp. 5525–5530, Nov. 2019.

[50] L. Miao, J. Shi, J. Yan, Y. Liu, X. Shu, and S. Che, "Experimental study and analysis of high sensitivity interferometric fiber optic gyroscope using multi-core fiber," *Opt. Fiber Technol.*, vol. 73, Oct. 2022, Art. no. 103052.

[51] H. Gap Park, M. Digonnet, and G. Kino, "Er-doped superfluorescent fiber source with a±0.5-ppm long-term mean-wavelength stability," *J. Lightw. Technol.*, vol. 21, no. 12, pp. 3427–3433, Dec. 2003.

[52] T. P. Gaiffe, P. Simonpietri, J. Morisse, N. Cerre, E. M. Taufflieb, and H. C. Lefevre, "Wavelength stabilization of an erbium-doped fiber source with a fiber Bragg grating for high-accuracy FOG," in *Proc. Fiber Optic Gyros, 20th Anniversary Conf.*, Denver, CO, USA, Nov. 1996, pp. 375–380.

[53] Y. Liu et al., "A photonic integrated circuit-based erbium-doped amplifier," *Science*, vol. 376, no. 6599, pp. 1309–1313, Jun. 2022.

[54] K. Böhm, P. Marten, K. Petermann, E. Weidel, and R. Ulrich, "Low-drift fibre gyro using a superluminescent diode," *Electron. Lett.*, vol. 17, no. 10, p. 352, 1981.

[55] P. F. Wysocki, M. J. F. Digonnet, B. Y. Kim, and H. J. Shaw, "Erbium-doped superfluorescent fiber sources have characteristics that make them ideal for interferometric sensor applications," *J. Lightw. Technol.*, vol. 12, no. 3, pp. 550–567, Mar. 1994.

[56] T. Komljenovic, M. A. Tran, M. Belt, S. Gundavarapu, D. J. Blumenthal, and J. E. Bowers, "Frequency modulated lasers for interferometric optical gyroscopes," *Opt. Lett.*, vol. 41, no. 8, p. 1773, Apr. 2016.

[57] J. Chamoun and M. J. F. Digonnet, "Pseudo-random-bit-sequence phase modulation for reduced errors in a fiber optic gyroscope," *Opt. Lett.*, vol. 41, no. 24, p. 5664, Dec. 2016.

[58] J. M. Wheeler and M. J. F. Digonnet, "A low-drift laser-driven FOG suitable for trans-pacific inertial navigation," *J. Lightw. Technol.*, vol. 40, no. 22, pp. 7464–7470, Nov. 2022.

[59] L. M. Augustin et al., "InP-based generic foundry platform for photonic integrated circuits," *IEEE J. Sel. Topics Quantum Electron.*, vol. 24, no. 1, pp. 1–10, Jan. 2018.

[60] F. M. Soares et al., "InP-based foundry PICs for optical interconnects," *Appl. Sci.*, vol. 9, no. 8, p. 1588, Apr. 2019.

[61] Y.-C. Wang, R.-Y. Liu, and Y.-J. Hung, "Monolithic InP-based optical driver chip for interferometric optical gyroscopes," prsented at the Opt. Photon. Taiwan, Int. Conf. (OPTIC), Kaohsiung, Taiwan, 2017.

[62] S. Stopinski, A. Jusza, and R. Piramidowicz, "Photonic integrated circuits for application in modern inertial measurement units," in *Proc. Baltic URSI Symp. (URSI)*, Poznan, Poland, May 2018, pp. 27–28.

[63] X. Dai et al., "High performance InP-based polarization beam splitter with reverse bias and injection current," *J. Lightw. Technol.*, vol. 38, no. 8, pp. 2336–2345, Apr. 2020.

[64] X. Dai, G. Zhao, Q. Chen, Q. Lu, J. F. Donegan, and W. Guo, "High-performance InP-based Mach–Zehnder polarization beam splitter with a 19 dB extinction ratio across C-band," *Opt. Lett.*, vol. 44, no. 17, pp. 4299–4302, 2019.

[65] N. Abadía et al., "Highly fabrication tolerant InP based polarization beam splitter based on p-i-n structure," *Opt. Exp.*, vol. 25, no. 9, 2017, Art. no. 10070.

[66] N. M. Fahrenkopf, C. McDonough, G. L. Leake, Z. Su, E. Timurdogan, and D. D. Coolbaugh, "The AIM photonics MPW: A highly accessible cutting edge technology for rapid prototyping of photonic integrated circuits," *IEEE J. Sel. Topics Quantum Electron.*, vol. 25, no. 5, pp. 1–6, Sep. 2019.

[67] M. Pantouvaki et al., "Active components for 50 Gb/s NRZ-OOK optical interconnects in a silicon photonics platform," *J. Lightw. Technol.*, vol. 35, no. 4, pp. 631–638, Feb. 2017.

[68] K. Giewont et al., "300-mm monolithic silicon photonics foundry technology," *IEEE J. Sel. Topics Quantum Electron.*, vol. 25, no. 5, pp. 1–11, Sep. 2019.

[69] R. Marchetti et al., "High-efficiency grating-couplers: Demonstration of a new design strategy," *Sci. Rep.*, vol. 7, no. 1, Nov. 2017, Art. no. 16670.

[70] L. Wang, D. R. Halstead, T. D. Monte, J. A. Khan, J. Brunner, and M. A. K. van Heyningen, "Low-cost, high-end tactical-grade fiber optic gyroscope based on photonic integrated circuit," in *Proc. IEEE Int. Symp. Inertial Sensors Syst. (INERTIAL)*, Naples, FL, USA, Apr. 2019, pp. 1–2.

[71] Y.-C. Wang et al., "Silicon photonics multi-function integrated optical circuit for miniaturized fiber optic gyroscope," *J. Lightw. Technol.*, vol. 41, no. 19, pp. 6324–6332, Oct. 2023.

[72] Y.-J. Hung, "Silicon photonic integrated circuit and fiber optic gyroscope apparatus using grating couplers," U.S. Patent 11 313 682, Apr. 26, 2022.

[73] A. W. Fang, H. Park, R. Jones, O. Cohen, M. J. Paniccia, and J. E. Bowers, "A continuous-wave hybrid AlGaInAs-silicon evanescent laser," *IEEE Photon. Technol. Lett.*, vol. 18, no. 10, pp. 1143–1145, May 2006.

[74] T. Komljenovic et al., "Heterogeneous silicon photonic integrated circuits," *J. Lightw. Technol.*, vol. 34, no. 1, pp. 20–35, Jan. 2016.

[75] A. Lee, Q. Jiang, M. Tang, A. Seeds, and H. Liu, "Continuous-wave InAs/GaAs quantum-dot laser diodes monolithically grown on Si substrate with low threshold current densities," *Opt. Exp.*, vol. 20, no. 20, 2012, Art. no. 22181.

[76] M. A. Tran, T. Komljenovic, J. C. Hulme, M. Kennedy, D. J. Blumenthal, and J. E. Bowers, "Integrated optical driver for interferometric optical gyroscopes," *Opt. Exp.*, vol. 25, no. 4, p. 3826, 2017.

[77] H.-W. Chen, Y.-H. Kuo, and J. E. Bowers, "A hybrid silicon–AlGaInAs phase modulator," *IEEE Photon. Technol. Lett.*, vol. 20, no. 23, pp. 1920–1922, Dec. 2008.

[78] A. De Groote et al., "Heterogeneously integrated III–V-on-silicon multibandgap superluminescent light-emitting diode with 290 nm optical bandwidth," *Opt. Lett.*, vol. 39, no. 16, pp. 4784–4787, 2014.

[79] K. Mehta et al., "High-power heterogeneously integrated III-V/silicon superluminescent diode," *IEEE Photon. Technol. Lett.*, vol. 35, no. 7, pp. 365–368, Apr. 2023.

[80] F. Zhang, H. Yun, Y. Wang, Z. Lu, L. Chrostowski, and N. A. F. Jaeger, "Compact broadband polarization beam splitter using a symmetric directional coupler with sinusoidal bends," *Opt. Lett.*, vol. 42, no. 2, p. 235, 2017.

[81] H. Xu, D. Dai, and Y. Shi, "Ultra-broadband and ultra-compact on-chip silicon polarization beam splitter by using hetero-anisotropic metamaterials," *Laser Photon. Rev.*, vol. 13, no. 4, 2019, Art. no. 1800349.

[82] C. Ciminelli et al., "A high-Q InP resonant angular velocity sensor for a monolithically integrated optical gyroscope," *IEEE Photon. J.*, vol. 8, no. 1, pp. 1–19, Feb. 2016.

[83] D. D'Agostino et al., "Low-loss passive waveguides in a generic InP foundry process via local diffusion of zinc," *Opt. Exp.*, vol. 23, no. 19, pp. 25143–25157, 2015.

[84] B. Wu, Y. Yu, J. Xiong, and X. Zhang, "Silicon integrated interferometric optical gyroscope," *Sci. Rep.*, vol. 8, no. 1, p. 8766, Jun. 2018.

[85] A. Biberman, M. J. Shaw, E. Timurdogan, J. B. Wright, and M. R. Watts, "Ultralow-loss silicon ring resonators," *Opt. Lett.*, vol. 37, no. 20, p. 4236, 2012.

[86] M. Tran, D. Huang, T. Komljenovic, J. Peters, A. Malik, and J. Bowers, "Ultra-low-loss silicon waveguides for heterogeneously integrated silicon/III-V photonics," *Appl. Sci.*, vol. 8, no. 7, p. 1139, Jul. 2018.

[87] M. L. Davenport, S. Skendžic, N. Volet, J. C. Hulme, M. J. R. Heck, and J. E. Bowers, "Heterogeneous silicon/III–V semiconductor optical amplifiers," *IEEE J. Sel. Topics Quantum Electron.*, vol. 22, no. 6, pp. 78–88, Nov. 2016.

[88] S. Gundavarapu et al., "Interferometric optical gyroscope based on an integrated Si3N4 low-loss waveguide coil," *J. Lightw. Technol.*, vol. 36, no. 4, pp. 1185–1191, Feb. 2018.

[89] D. Liu et al., "Interferometric optical gyroscope based on an integrated silica waveguide coil with low loss," *Opt. Exp.*, vol. 28, no. 10, pp. 15718–15730, 2020.

[90] J. Bauters et al., "Planar waveguides with less than 0.1 dB/m propagation loss fabricated with wafer bonding," *Opt. Exp.*, vol. 19, no. 24, pp. 24090–24101, 2011.

[91] T. Huffman, M. Davenport, M. Belt, J. E. Bowers, and D. J. Blumenthal, "Ultra-low loss large area waveguide coils for integrated optical gyroscopes," *IEEE Photon. Technol. Lett.*, vol. 29, no. 2, pp. 185–188, Jan. 2017.

[92] M. Horton, "Planar silicon nitride waveguide and silicon photonics integrated circuit for commercial optical gyroscope," *Proc. SPIE*, vol. PC12105, Jun. 2022.

[93] M. Paniccia and Q. Tan, "System architecture for integrated photonics optical gyroscopes," U.S. Patent 10 731 988, Aug. 4, 2020.

[94] M. Paniccia and A. Feshali, "Single-layer and multi-layer structures for integrated silicon photonics optical gyroscopes," U.S. Patent 11 119 276, Sep. 14, 2021.

[95] C. L. Garrido Alzar, "Compact chip-scale guided cold atom gyrometers for inertial navigation: Enabling technologies and design study," *AVS Quantum Sci.*, vol. 1, no. 1, Dec. 2019, Art. no. 014702.

[96] M. J. Grant and M. J. F. Digonnet, "Rotation sensitivity and shot-noise-limited detection in an exceptional-point coupled-ring gyroscope," *Opt. Lett.*, vol. 46, no. 12, pp. 2936–2939, Jun. 2021.

[97] A. D. Challoner, H. H. Ge, and J. Y. Liu, "Boeing disc resonator gyroscope," in *Proc. IEEE/ION Position, Location Navigat. Symp. (PLANS)*, May 2014, pp. 504–514.

[98] P. Wang et al., "Calibration of coupling errors for scale factor nonlinearity improvement in navigation-grade honeycomb disk resonator gyroscope," *IEEE Trans. Ind. Electron.*, vol. 70, no. 5, pp. 5347–5355, May 2023.

[99] S. Koenig et al., "Towards a navigation grade Si-MEMS gyroscope," in *Proc. DGON Inertial Sensors Syst. (ISS)*, Sep. 2019, pp. 1–18.

[100] D. Endean et al., "Near-navigation grade tuning fork MEMS gyroscope," in *Proc. IEEE Int. Symp. Inertial Sensors Syst. (INERTIAL)*, Apr. 2019, pp. 1–4.

[101] A. Buffoli, M. Gadola, M. Sansa, and G. Langfelder, "0.02 °/h, 0.004°/vh, 6.3-mA NEMS gyroscope with integrated circuit," *IEEE Trans. Instrum. Meas.*, vol. 72, pp. 1–8, 2023.

[102] S. Kowaltschek, "Lessons learnt from the sireus MEMS detector evaluation," in *Proc. 6th ESA/ESTEC Workshop Avionics Data, Control Softw. Syst.*, pp. 1–16, 2012.

[103] M. Faucheux, D. Fayoux, and J. J. Roland, "The ring laser gyro," *J. Opt.*, vol. 19, pp. 101–115, May 1988.

[104] Y.-H. Lai et al., "Earth rotation measured by a chip-scale ring laser gyroscope," *Nature Photon.*, vol. 14, no. 6, pp. 345–349, Jun. 2020.

[105] G. A. Sanders, L. K. Strandjord, W. Williams, E. Benser, S. Ayotte, and F. Costin, "Improvements to signal processing and component minaturization of compact resonator fiber optic gyroscopes," in *Proc. DGON Inertial Sensors Syst. (ISS)*, Braunschweig, Germany, Sep. 2018, pp. 1–22.

[106] S. Zhao, Q. Liu, Y. Liu, H. Ma, and Z. He, "Navigation-grade resonant fiber-optic gyroscope using ultra-simple white-light multibeam interferometry," *Photon. Res.*, vol. 10, no. 2, p. 542, Feb. 2022.

[107] J. Hu, S. Liu, L. Liu, and H. Ma, "Closed-loop resonant fiber-optic gyroscope with a broadband light source," *J. Lightw. Technol.*, vol. 41, no. 18, pp. 6088–6093, Sep. 2023.

[108] S. Ferrand et al., "UmiX series: How to miniaturize FOG technology," in *Proc. IEEE Int. Symp. Inertial Sensors Syst. (INERTIAL)*, Avignon, France, May 2022, pp. 1–4.

[109] Z. Wang, G. Wang, S. Kumar, C. Marques, R. Min, and X. Li, "Recent advancements in resonant fiber optic gyro—A review," *IEEE Sensors J.*, vol. 22, no. 19, pp. 18240–18252, Oct. 2022.

[110] W. Liang et al., "Resonant microphotonic gyroscope," *Optica*, vol. 4, no. 1, p. 114, Jan. 2017.

[111] A. B. Matsko, W. Liang, A. A. Savchenkov, V. S. Ilchenko, and L. Maleki, "Fundamental limitations of sensitivity of whispering gallery mode gyroscopes," *Phys. Lett. A*, vol. 382, no. 33, pp. 2289–2295, Aug. 2018.

[112] A. Matsko, S. Vyatchanin, A. Savchenkov, and S. Williams, "Quantum limitations and back action evading measurements in classical force and rotation detection," in *Proc. SPIE*, vol. 10934, pp. 98–106, Mar. 2019.
[113] L. Meyer, B. C. GroverEdward, and K. G. MarkRoger, "Nuclear magnetic resonance gyro," U.S. Patent 4 157 495, Jun. 5, 1979.
[114] J. Kitching, "Chip-scale atomic devices," *Appl. Phys. Rev.*, vol. 5, no. 3, Sep. 2018, Art. no. 031302.
[115] T. G. Walker and M. S. Larsen, "Spin-exchange-pumped NMR gyros," *Adv. At., Mol., Opt. Phys.*, vol. 65, pp. 373–401, Jan. 2016.
[116] S. Karlen et al., "MEMS atomic vapor cells for gyroscope applications," in *Proc. Joint Conf. Eur. Freq. Time Forum IEEE Int. Freq. Control Symp. (EFTF/IFCS)*, Jul. 2017, pp. 315–316.
[117] M. P. Ledbetter, K. Jensen, R. Fischer, A. Jarmola, and D. Budker, "Gyroscopes based on nitrogen-vacancy centers in diamond," *Phys. Rev. A, Gen. Phys.*, vol. 86, no. 5, Nov. 2012, Art. no. 052116.
[118] A. Ajoy and P. Cappellaro, "Stable three-axis nuclear-spin gyroscope in diamond," *Phys. Rev. A, Gen. Phys.*, vol. 86, no. 6, Dec. 2012, Art. no. 062104.
[119] A. Jarmola et al., "Demonstration of diamond nuclear spin gyroscope," *Sci. Adv.*, vol. 7, no. 43, Oct. 2021, Art. no. eabl3840.
[120] L. Zhao, X. Shen, L. Ji, and P. Huang, "Inertial measurement with solid-state spins of nitrogen-vacancy center in diamond," *Adv. Phys., X*, vol. 7, no. 1, Dec. 2022, Art. no. 2004921.
[121] K. Schauble, M. Horton, and A. Photonics, "Extended indoor navigation using battery-operated optical gyroscope-based system," presented at the Joint Navigat. Conf., San Diego, CA, USA, Jun. 12–15, 2023.

Francesco Dell'Olio (Senior Member, IEEE) received the M.S. degree in electronic engineering and the Ph.D. degree from the Polytechnic University of Bari, Bari, Italy, in 2005 and 2010, respectively.

In 2015, he joined the Department of Electrical and Information Engineering, Polytechnic University of Bari, as an Assistant Professor, where he was promoted to an Associate Professor in 2022. He is the coauthor of two books, published by Springer and World Scientific, and more than 50 articles in international peer-reviewed journals. He has been involved in several research projects funded by the Italian Ministry of University and Research, the European Space Agency, the Italian Space Agency, and industrial companies, some of which involved taking on the role of principal investigator. His research focuses on silicon photonics and nanophotonics, with particular regard to modeling, design, and characterization of devices and integrated circuits for telecommunications and sensing. He has of late branched into electrochemical and colorimetric wearable sensors and miniature sensor-based embedded systems.

Mr. Dell'Olio is a regular member of organizing committees and program committees for international conferences, including Conference on Lasers and Electro-Optics (CLEO), Society of Photo-Optical Instrumentation Engineers (SPIE) Photonics West, and the IEEE Photonics Conference.

Teresa Natale was born in 1998. She received the M.S. degree in electronic engineering from the Polytechnic University of Bari, Bari, Italy, in 2022, where she is currently pursuing the Ph.D. degree in electrical and information engineering. Her M.S. thesis was partially carried out at the Physics Department, Biomolecular Photonics Laboratory, University of Bielefeld, Bielefeld, Germany.

Her research is focused on microphotonic sensors and the relevant readout electronic circuits.

Yen-Chieh Wang received the B.S. degree from the Department of Applied Materials and Optoelectronic Engineering, National Chi Nan University (NCCU), Nantou, Taiwan, in 2014, and the M.S. degree from the Department of Photonics, National Sun Yat-sen University (NSYSU), Kaohsiung, Taiwan, in 2016, where he is currently pursuing the Ph.D. degree.

He has been engaged in research on semiconductor distributed feedback lasers, silicon photonic integrated circuits, and fiber optic gyroscope.

Yung-Jr Hung (Member, IEEE) received the B.S. and Ph.D. degrees in electrical engineering from the National Taiwan University of Science and Technology (NTUST), Taipei, Taiwan, in 2005 and 2010, respectively.

He was a Visiting Scholar at the Department of Electrical and Computer Engineering, University of California at Santa Barbara, Santa Barbara, CA, USA, in 2009. In 2013, he joined the Department of Photonics, National Sun Yat-sen University (NSYSU), Kaohsiung, Taiwan, as an Assistant Professor, where he was promoted to a Professor in 2021. He has (co)authored over 200 technical journal articles and conference papers and holds ten patents. His current research interests are in the areas of silicon photonic integrated circuits, semiconductor laser, and fiber optic gyroscope.

Mr. Hung was a recipient of the IEEE Best Young Professional Member Award in 2019 and the MOST Da-You Wu Memorial Award in 2020. He was honored as the Distinguished Professor at NSYSU in 2023 for excellent academia–industrial cooperation.

Open Access funding provided by 'Politecnico di Bari' within the CRUI CARE Agreement